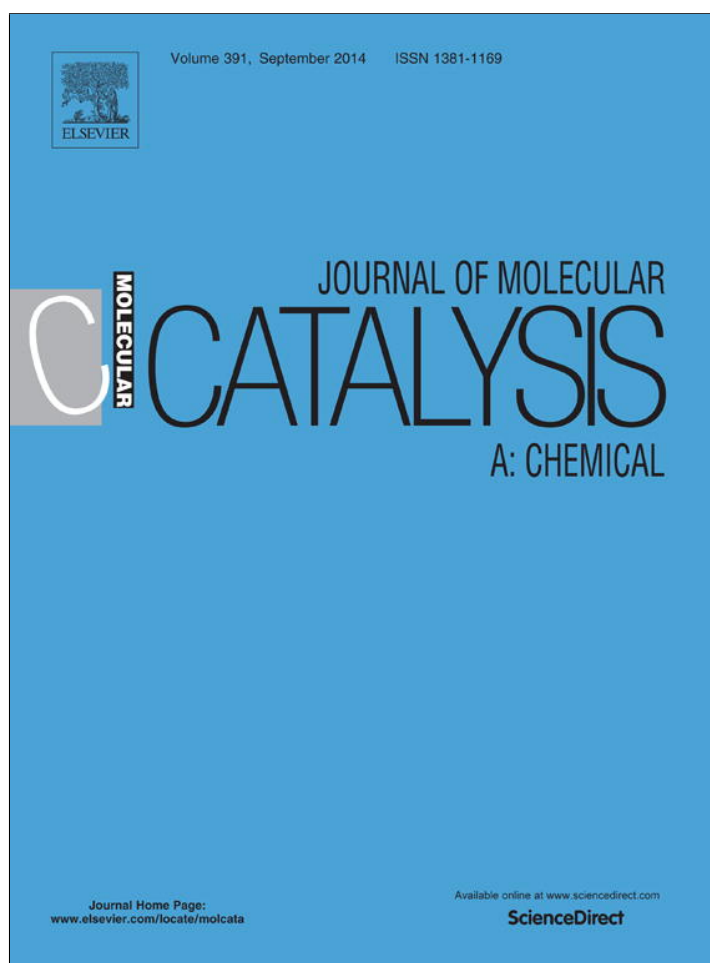


Provided for non-commercial research and education use.
Not for reproduction, distribution or commercial use.



This article appeared in a journal published by Elsevier. The attached copy is furnished to the author for internal non-commercial research and education use, including for instruction at the authors institution and sharing with colleagues.

Other uses, including reproduction and distribution, or selling or licensing copies, or posting to personal, institutional or third party websites are prohibited.

In most cases authors are permitted to post their version of the article (e.g. in Word or Tex form) to their personal website or institutional repository. Authors requiring further information regarding Elsevier's archiving and manuscript policies are encouraged to visit:

<http://www.elsevier.com/authorsrights>



Contents lists available at ScienceDirect

Journal of Molecular Catalysis A: Chemical

journal homepage: www.elsevier.com/locate/molcata

Synthesis, characterization, photocatalytic activity of visible-light-responsive photocatalysts $\text{BiO}_x\text{Cl}_y/\text{BiO}_m\text{Br}_n$ by controlled hydrothermal method



Shiuh-Tsuen Huang, Yu-Rou Jiang, Shang-Yi Chou, Yong-Ming Dai, Chiing-Chang Chen*

Department of Science Application and Dissemination, National Taichung University of Education, Taiwan

ARTICLE INFO

Article history:

Received 18 February 2014

Received in revised form 10 April 2014

Accepted 15 April 2014

Available online 24 April 2014

Keywords:

Photocatalytic
Bismuth oxyhalides
Heterojunction
Crystal violet
 $\text{BiO}_x\text{Cl}_y/\text{BiO}_m\text{Br}_n$

ABSTRACT

Bismuth oxyhalide and its composite belong to a new family of visible light driven photocatalysts and attract more and more attention because of their interesting structures dependent on the photocatalytic performance arisen from their layered structures interleaved with $[\text{Bi}_2\text{O}_2]$ slabs and double halogen atoms slabs. An effective and simple strategy to improve the photocatalytic activity of a photocatalyst is the construction of a heterostructure, as the heterojunction has great potential in tuning the desired electronic properties of the composite photocatalysts and efficiently separating the photogenerated electron–hole pairs. This is the first report that a series of $\text{BiO}_x\text{Cl}_y/\text{BiO}_m\text{Br}_n$ heterojunctions are prepared using controlled hydrothermal methods. The compositions and morphologies of $\text{BiO}_x\text{Cl}_y/\text{BiO}_m\text{Br}_n$ could be controlled by adjusting some growth parameters, including reaction pH, time, and temperature. The products are characterized by XRD, SEM-EDS, HR-TEM, DR-UV, BET, CL, and HR-XPS.

© 2014 Elsevier B.V. All rights reserved.

1. Introduction

Around 10^6 tons and more than 10,000 different synthetic dyes and pigments are produced annually worldwide, which are used extensively in dye and printing industries. It is estimated that about 10% of those are lost in industrial effluents [1]. Triphenylmethane (TPM) dyes are suitable for a large variety of technological applications. They are used extensively in textile industry for dyeing nylon, wool, cotton, and silk, as well as for coloring oil, fat, wax, varnish, and plastic. Paper, leather, cosmetic, and food industries are other major consumers of various TPM dyes [2,3]. Cationic TPM dyes are widely used as antimicrobial agents [3]. Recent reports indicated that they might further serve as targetable sensitizers in the photo-destruction of specific cellular components or cells [4,5]. Additionally, TPM dyes are used as staining agents in bacteriological and histopathological applications. The photo-cytotoxicity of TPM dyes based on reactive oxygen species production has been tested intensively with a view to developing a photodynamic therapy [6]. However, the thyroid peroxidase-catalyzed oxidation of TPM class of dyes is of great concern because the reactions might form

various *N*-de-alkylated primary and secondary aromatic amines, with structures similar to aromatic amine carcinogens [5].

Many alternative processes aiming at removing TPM from wastewater have been investigated, including chemical oxidation and reduction, physical precipitation and flocculation, photolysis, adsorption, electrochemical treatment, advanced oxidation, reverse osmosis and biodegradation [7]. The photocatalysis process has been successfully used for degrading TPM dye pollutants in the past few years [8,9]. Environmental pressure has impelled the search for new technological developments. CV has been studied in several hydroxyl radical ($\cdot\text{OH}$) generating systems, including TiO_2 [10], modified- TiO_2 [11,12], ZnO [13,14], Bi_2WO_6 [15,16], BaTiO_3 [17], Fe_2O_3 [18], $\text{Bi}_x\text{Ag}_y\text{O}_z$ [19], and Fe^{2+} or $\text{Fe}^{3+}/\text{H}_2\text{O}_2$ [20,21]. In most cases, the reaction mechanisms, kinetics, and/or efficiency are well documented.

The photocatalytic activity of TiO_2 in visible light is very low due to its wide band gap, preventing it from the efficient absorption of sunlight. Recently, the development of visible light sensitive photocatalysts has received considerable attention as an alternative treatment of wastewater. Bismuth oxyhalides, a group of V–VI–VII semiconductors of great importance due to their superior optical properties and promising industrial applications, have been used as catalysts, ferroelectric materials, and pigments etc. [22]. Bismuth oxyhalides belong to a new family of visible light driven photocatalysts and attract more and more attention because of

* Corresponding author. Tel.: +886 4 2218 3406; fax: +886 4 2218 356.

E-mail addresses: ccchen@mail.ntcu.edu.tw, ccchen@ms3.ntcu.edu.tw (C.-C. Chen).

their interesting structures dependent on the photocatalytic performance arisen from their layered structures interleaved with $[\text{Bi}_2\text{O}_2]$ slabs and double halogen atoms slabs [23,24]. The formed internal electric fields between the $[\text{Bi}_2\text{O}_2]^{2+}$ positive layer and the negative halogen layer could induce an efficient separation of photogenerated electron–hole pairs thus enhancing the photocatalytic activities of the catalysts [25].

An effective and simple strategy to improve the photocatalytic activity of a photocatalyst is the construction of a heterostructure, as the heterojunction has great potential in tuning the desired electronic properties of the composite photocatalysts and efficiently separating the photogenerated electron–hole pairs [26,27]. Following Keller et al. [28] who first reported the practically unlimited solubility of the BiOX/BiOY ($X, Y = \text{Cl}, \text{Br}, \text{I}$) systems, several articles were published to disclose the successful synthesis and the unique photocatalytic properties of similar oxyhalide materials. Wang et al. [29] reported the synthesis of BiOI/BiOCl and BiOBr/BiOI phases exhibiting high photocatalytic activities under visible light irradiation for the degradation of methyl orange. Shenawi-Khalil et al. [30] prepared $\text{BiO}(\text{Cl}_x\text{Br}_{1-x})$ photocatalysts by a hydrothermal method and found that the new photoactive material with $x = 0.5$ demonstrated 3 times higher rate than Degussa P25 did in removing aqueous RhB under visible light irradiation. Recently, Zhang et al. [31] developed a facile reactable ionic-liquid synthesis of $\text{BiOCl}/\text{BiOBr}$ flower-like microspheres by an EG-assisted solvothermal process. The DRS analysis and high photocurrent suggested that $\text{BiOCl}/\text{BiOBr}$ possessed the absorption under visible light and was a benefit for the efficient generation and separation of the electron–hole pairs.

The present work reports the preparation and characterization of a new family of $\text{BiO}_x\text{Cl}_y/\text{BiO}_m\text{Br}_n$ photocatalysts. This is the first report demonstrating the synthesis study of $\text{BiO}_x\text{Cl}_y/\text{BiO}_m\text{Br}_n$ photocatalysts by controlled hydrothermal methods. The photocatalytic activities of the new materials being evaluated by measuring the degradation rate of CV under visible light irradiation have an excellent activity. In comparison to BiOCl and BiOBr , the new photoactive material demonstrates higher rate in removing aqueous CV under visible light irradiation.

2. Materials and methods

2.1. Material

The purchased KBr (Katayama), KCl (Shimakyu), $\text{Bi}(\text{NO}_3)_3 \cdot 5\text{H}_2\text{O}$, and CV dye (TCI) were obtained and used without any further purification. Reagent-grade nitric acid, sodium hydroxide, ammonium acetate, and HPLC-grade methanol were obtained from Merck. The de-ionized water used in this study was purified with a Milli-Q water ion-exchange system (Millipore Co.) for a resistivity of $1.8 \times 10^7 \Omega\text{-cm}$.

2.2. Instruments and analytical methods

XRD patterns were recorded on a MAC Science, MXP18 X-ray diffractometer with $\text{Cu K}\alpha$ radiation, and operated at 40 kV and 80 mA. The field-emission transmission electron microscopy (FE-TEM) images, SAED pattern, high-resolution transmission electron microscopy (HRTEM) images and an energy-dispersive X-ray spectrum (EDS) were taken on a JEOL-2010 transmission electron microscope with an accelerating voltage of 200 kV. FE-SEM-EDS measurements were carried out with a field-emission microscope (JEOL JSM-7401F) at an acceleration voltage of 15 kV and an HRXPS measurement was carried out with ULVAC-PHI XPS. The Al $\text{K}\alpha$ radiation was generated with a voltage of 15 kV. The BET specific surface areas of the samples were measured with an automatic system

(Micromeritics Gemini 237 °C) using nitrogen gas as the adsorbate, at liquid nitrogen temperature. Cryogenic cathodoluminescence (CL) measurements were carried out on JEOL JSM7001F.

The HPLC-PDA-ESI-MS system consisted of a Waters 1525 binary pump, a 2998 photodiode array detector, and a 717 plus autosampler. Besides, a ZQ2000 micromass detector and an AtlantisTM dC18 column (250 mm \times 4.6 mm i.d., $\text{dp} = 5 \mu\text{m}$) were used for separation and identification. The column effluent was introduced into the ESI source of the mass spectrometer.

The amount of residual dye at each reaction cycle was determined by HPLC-PDA-ESI-MS. The analysis of organic intermediates was accomplished by HPLC-PDA-ESI-MS after the readjustment of chromatographic conditions in order to make the mobile phase (Solvent A and B) compatible with the working conditions of the mass spectrometer. Solvent A was 25 mM aqueous ammonium acetate buffer (pH 6.9), and solvent B was methanol. LC was carried out on an AtlantisTM dC18 column (250 mm \times 4.6 mm i.d., $\text{dp} = 5 \mu\text{m}$). The mobile phase flow rate was 1.0 mL/min. A linear gradient was run as follows: $t = 0, A = 95, B = 5$; $t = 20, A = 50, B = 50$; $t = 35\text{--}40, A = 10, B = 90$; $t = 45, A = 95, B = 5$. The column effluent was introduced into the ESI source of the mass spectrometer. The quadruple mass spectrometer equipped with an ESI interface with heated nebulizer probe at 350 °C was used with an ion source temperature of 80 °C. ESI was carried out with the vaporizer at 350 °C and nitrogen as sheath (80 psi) and auxiliary (20 psi) gas to assist with the preliminary nebulization and to initiate the ionization process. A discharge current of 5 μA was applied. Tube lens and capillary voltage were optimized for the maximum response during the perfusion of the CV standard.

2.3. Synthesis of $\text{BiO}_x\text{Cl}_y/\text{BiO}_m\text{Br}_n$

5 mmol $\text{Bi}(\text{NO}_3)_3 \cdot 5\text{H}_2\text{O}$ was first mixed in a 50 mL flask and followed by adding 5 mL 4 M HNO_3 . With continuous stirring, 2 M NaOH was added dropwise to adjust the pH value; and, when a precipitate was formed, 2 mL KCl and KBr were also added dropwise. The solution was then stirred vigorously for 30 min and transferred into a 30 mL Teflon-lined autoclave, which was heated up to 110–260 °C for 12, 24, and 36 h and then naturally cooled down to room temperature. The resulting solid product was collected by filtration, washed with deionized water and methanol to remove any possible ionic species in the product, and then dried at 60 °C overnight. A variety of reaction conditions in hydrothermal methods were employed (including Cl/Br mole ratio, pH value, temperatures, and times) as shown the catalyst codes in Table 1, namely BC1B2-1-110-12 (Cl:Br = 1:2 molar ratio) to BC2B1-260-24 (Cl:Br = 2:1 molar ratio) for as-prepared samples, respectively.

2.4. Evaluation of photocatalytic activity

The aqueous suspension of CV (100 mL, 10 ppm) and the amount of catalyst powder were placed in the Pyrex flask. The pH value of the suspension was adjusted by adding either NaOH or HNO_3 solution. Prior to irradiation, the suspension was magnetically stirred in the dark for ca. 30 min to establish adsorption/desorption equilibrium between the dye and the surface of the catalyst under ambient air-equilibrated conditions. The irradiation was carried out using visible-light lamps (500 W Xe arc). The light intensity was fixed on 132.1 W/m^2 when the reactor was placed 30 cm away from the light source. The irradiation experiments of CV were carried out on stirred aqueous solution contained in a 100 mL flask. At the given irradiation time intervals, 5 mL aliquot was collected and centrifuged to remove the catalyst. The supernatant was analyzed by HPLC-ESI-MS after readjusting the chromatographic conditions

Table 1Codes of $\text{BiO}_x\text{Cl}_y/\text{BiO}_m\text{Br}_n$ prepared under different KCl/KBr molar ratio, pH values, and reaction temperatures at 12 h. (BC1B2, Cl:Br = 1:2; BC2B1, Cl:Br = 2:1).

pH	Temp (°C)			
	110	160	210	260
BC1B2				
1	BC1B2-1-110-12	BC1B2-1-160-12	BC1B2-1-210-12	BC1B2-1-260-12
4	BC1B2-4-110-12	BC1B2-4-160-12	BC1B2-4-210-12	BC1B2-4-260-12
7	BC1B2-7-110-12	BC1B2-7-160-12	BC1B2-7-210-12	BC1B2-7-260-12
10	BC1B2-10-110-12	BC1B2-10-160-12	BC1B2-10-210-12	BC1B2-10-260-12
13	BC1B2-13-110-12	BC1B2-13-160-12	BC1B2-13-210-12	BC1B2-13-260-12
BC2B1				
1	BC2B1-1-110-12	BC2B1-1-160-12	BC2B1-1-210-12	BC2B1-1-260-12
4	BC2B1-4-110-12	BC2B1-4-160-12	BC2B1-4-210-12	BC2B1-4-260-12
7	BC2B1-7-110-12	BC2B1-7-160-12	BC2B1-7-210-12	BC2B1-7-260-12
10	BC2B1-10-110-12	BC2B1-10-160-12	BC2B1-10-210-12	BC2B1-10-260-12
13	BC2B1-13-110-12	BC2B1-13-160-12	BC2B1-13-210-12	BC2B1-13-260-12

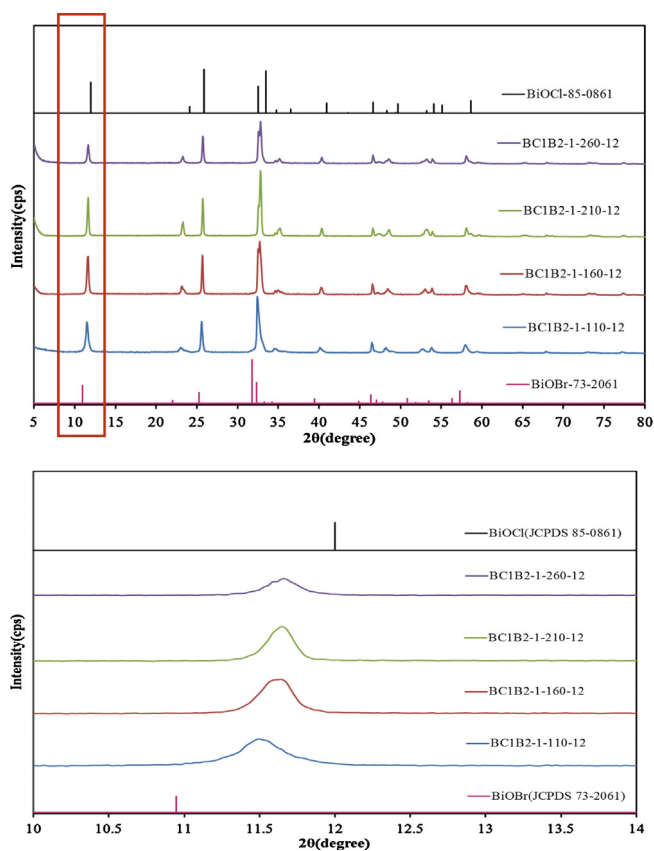


Fig. 1. (a) XRD patterns of as-prepared $\text{BiO}_x\text{Cl}_y/\text{BiO}_m\text{Br}_n$ samples under different synthesis temperature and (b) enlarged view of the diffraction region between 10 and 14°. (Molar ratio KCl/KBr = 1/2, hydrothermal conditions: temp = 110–260 °C, pH = 1, time = 12 h).

in order to make the mobile phase compatible with the working conditions of the mass spectrometer.

3. 3 Results and discussion

3.1. Characterization of the $\text{BiO}_x\text{Cl}_y/\text{BiO}_m\text{Br}_n$

3.1.1. XRD analysis

Figs. 1–4 and Figs. S1–S6 show the XRD patterns of the as-prepared $\text{BiO}_x\text{Cl}_y/\text{BiO}_m\text{Br}_n$ samples. The XRD patterns clearly revealed the existence of the pure phase and the coexistence of different phases. All the $\text{BiO}_x\text{Cl}_y/\text{BiO}_m\text{Br}_n$ samples synthesized using the hydrothermal method described at different

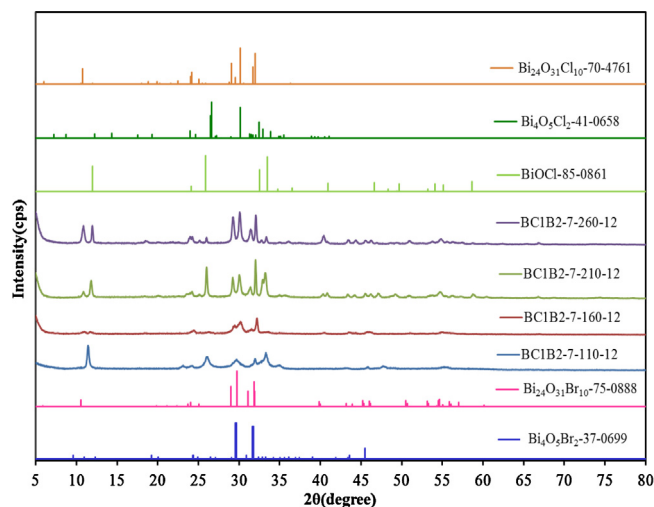


Fig. 2. XRD patterns of as-prepared $\text{BiO}_x\text{Cl}_y/\text{BiO}_m\text{Br}_n$ samples under different hydrothermal condition. (Molar ratio KCl/KBr = 1/2, temp = 110–260 °C, pH = 7, time = 12 h).

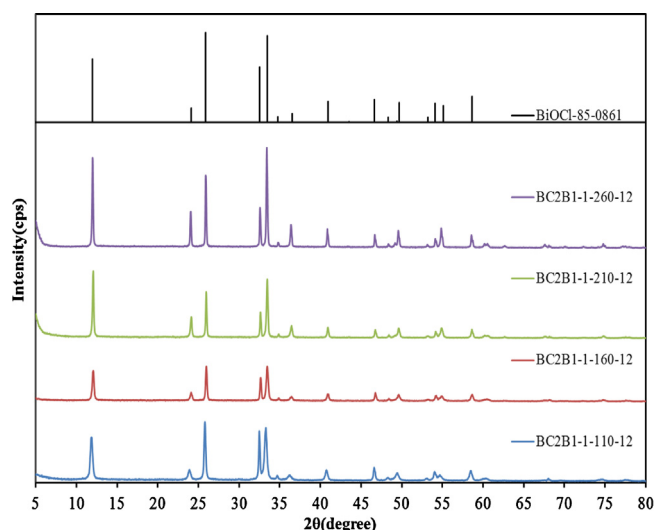


Fig. 3. XRD patterns of as-prepared $\text{BiO}_x\text{Cl}_y/\text{BiO}_m\text{Br}_n$ samples under different hydrothermal condition. (Molar ratio KCl/KBr = 2, temp = 110–260 °C, pH = 10, time = 12 h).

temperature and pH were BiOCl (JCPDS 85-0861), $\text{Bi}_4\text{O}_5\text{Cl}_2$ (JCPDS 41-0658), $\text{Bi}_{24}\text{O}_{31}\text{Cl}_{10}$ (JCPDS 70-4761), $\text{Bi}_3\text{O}_4\text{Cl}$ (JCPDS 36-0760), $\text{Bi}_{12}\text{O}_{17}\text{Cl}_2$ (JCPDS 37-0702), BiOBr (JCPDS 09-0393), $\text{Bi}_4\text{O}_5\text{Br}_2$ (JCPDS 37-0669), $\text{Bi}_{24}\text{O}_{31}\text{Br}_{10}$ (JCPDS 75-0888), $\text{Bi}_3\text{O}_4\text{Br}$

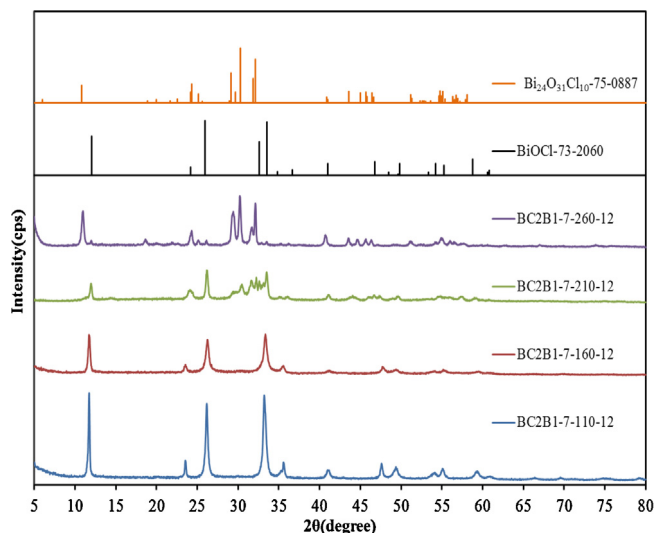


Fig. 4. XRD patterns of as-prepared $\text{BiO}_x\text{Cl}_y/\text{BiO}_m\text{Br}_n$ samples under different hydrothermal condition. (Molar ratio $\text{KCl}/\text{KBr}=2$, temp = 110–260 °C, pH = 7, time = 12 h).

(JCPDS 84-0793), $\text{Bi}_5\text{O}_7\text{Br}$ (JCPDS 38-0493), $\text{Bi}_{12}\text{O}_{17}\text{Br}_2$ (JCPDS 37-0701), and $\alpha\text{-Bi}_2\text{O}_3$ (JCPDS 41-1449) phase. The XRD patterns for pH = 1, 4, 7, 10, and 13 were identical to those reported for BiOCl and $\alpha\text{-Bi}_2\text{O}_3$ single phase, $\text{BiO}(\text{Cl}_x\text{Br}_{1-x})$ solid solution (Fig. 1) [28], $\text{BiOCl}/\text{BiOBr}$, $\text{Bi}_{24}\text{O}_{31}\text{Cl}_{10}/\text{Bi}_{24}\text{O}_{31}\text{Br}_{10}$, $\text{Bi}_3\text{O}_4\text{Cl}/\text{Bi}_{24}\text{O}_{31}\text{Br}_{10}$, $\text{Bi}_{12}\text{O}_{17}\text{Cl}_2/\text{Bi}_{24}\text{O}_{31}\text{Br}_{10}$, $\text{Bi}_{24}\text{O}_{31}\text{Cl}_{10}/\text{Bi}_{12}\text{O}_{17}\text{Br}_2$, $\text{Bi}_3\text{O}_4\text{Cl}/\text{Bi}_{12}\text{O}_{17}\text{Br}_2$ binary phase, and $\text{BiOCl}/\text{Bi}_4\text{O}_5\text{Cl}_2/\text{Bi}_4\text{O}_5\text{Br}_2$, $\text{BiOCl}/\text{Bi}_{24}\text{O}_{31}\text{Cl}_{10}/\text{BiOBr}$ ternary phase. Table 2 summarizes the results of the XRD measurements. In this experiment, pH and temperature play key roles in controlling the composition and anisotropic growth of crystals. The results showed that a series of changes in the compounds occurred at different pH values and hydrothermal reactions, described as $\text{BiOCl} \rightarrow \text{Bi}_4\text{O}_5\text{Cl}_2 \rightarrow \text{Bi}_{24}\text{O}_{31}\text{Cl}_{10} \rightarrow \text{Bi}_3\text{O}_4\text{Cl} \rightarrow \text{Bi}_{12}\text{O}_{17}\text{Cl}_2 \rightarrow \alpha\text{-Bi}_2\text{O}_3$ and $\text{BiOBr} \rightarrow \text{Bi}_4\text{O}_5\text{Br}_2 \rightarrow \text{Bi}_{24}\text{O}_{31}\text{Br}_{10} \rightarrow \text{Bi}_3\text{O}_4\text{Br} \rightarrow \text{Bi}_5\text{O}_7\text{Br} \rightarrow \text{Bi}_{12}\text{O}_{17}\text{Br}_2 \rightarrow \alpha\text{-Bi}_2\text{O}_3$. The possible processes for the formation of $\text{BiO}_x\text{Cl}_y/\text{BiO}_m\text{Br}_n$ samples are described as follows (Eqs. (1)–(18)).

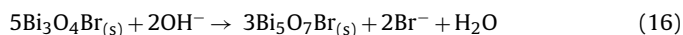
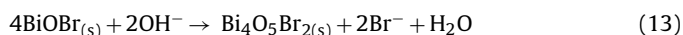
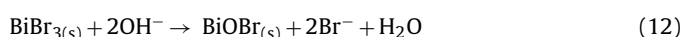
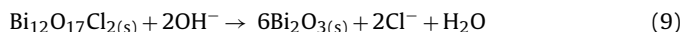
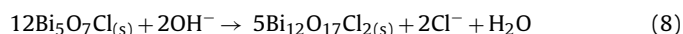
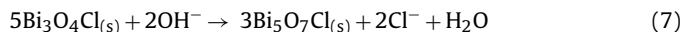
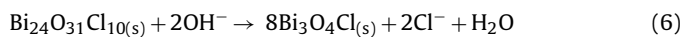
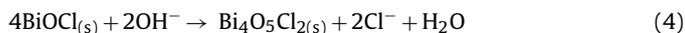
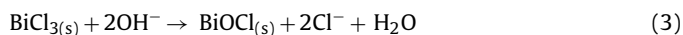
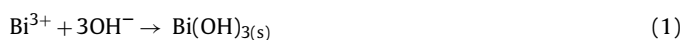
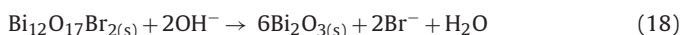


Table 2

Crystalline phase changes of binary bismuth oxyhalides nanosheets prepared under different pH value and reaction conditions. (● BiOBr ; ■ $\text{Bi}_4\text{O}_5\text{Br}_2$; ▲ $\text{Bi}_{24}\text{O}_{31}\text{Br}_{10}$; ● $\text{Bi}_{12}\text{O}_{17}\text{Br}_2$; ○ BiOCl ; □ $\text{Bi}_4\text{O}_5\text{Cl}_2$; ▲ $\text{Bi}_{24}\text{O}_{31}\text{Cl}_{10}$; ◆ $\text{Bi}_3\text{O}_4\text{Cl}$; ○ $\text{Bi}_{12}\text{O}_{17}\text{Cl}_2$; ★ $\alpha\text{-Bi}_2\text{O}_3$).

BC1B2				
pH	Temp(°C)			
	110	160	210	260
1	●○	●○	●○	●○
4	●○	●○	▲▲	▲▲
7	■□	■▲	■▲	■▲
10	▲◆	▲◆	▲◆	▲○
13	★	★	★	★
BC2B1				
pH	Temp(°C)			
	110	160	210	260
1	○	○	○	○
4	●○	●○	●○	●○
7	●○	●○	○▲	○▲
10	●▲	●▲	●◆	●◆
13	★	★	★	★



These equations showed that BiOCl (or BiOBr) was formed at the beginning of the reaction and then OH^- gradually substituted Cl^- (or Br^-) in the basic conditions, which resulted in the reduced content of Cl^- (or Br^-) in the products. Increasing the pH gradually to obtain $\text{Bi}_4\text{O}_5\text{Cl}_2$ (or $\text{Bi}_4\text{O}_5\text{Br}_2$), $\text{Bi}_{24}\text{O}_{31}\text{Cl}_{10}$ (or $\text{Bi}_{24}\text{O}_{31}\text{Br}_{10}$), $\text{Bi}_3\text{O}_4\text{Cl}$ (or $\text{Bi}_3\text{O}_4\text{Br}$), $\text{Bi}_5\text{O}_7\text{Cl}$ ($\text{Bi}_5\text{O}_7\text{Br}$), $\text{Bi}_{12}\text{O}_{17}\text{Cl}_2$ ($\text{Bi}_{12}\text{O}_{17}\text{Br}_2$), and $\alpha\text{-Bi}_2\text{O}_3$, the higher the pH value, the lower the Cl^- (or Br^-) content was in the products, until the content of Cl^- (or Br^-) in the products was fully replaced by OH^- , finally resulting in the formation of $\alpha\text{-Bi}_2\text{O}_3$ under strong basic conditions. However, BiOCl and $\alpha\text{-Bi}_2\text{O}_3$ were the exclusive products at pH 1 and 13. A competitive relationship typically existed between OH^- , Cl^- , and Br^- in aqueous solution. It demonstrated that $\text{BiO}_x\text{Cl}_y/\text{BiO}_m\text{Br}_n$ could be selectively prepared through adjusted pH values under the hydrothermal method.

3.1.2. FE-SEM-EDS and FE-TEM-EDS analysis

$\text{BiO}_x\text{Cl}_y/\text{BiO}_m\text{Br}_n$ was prepared with $\text{Bi}(\text{NO}_3)_3 \cdot 5\text{H}_2\text{O}$ and the mixture of KCl and KBr by the hydrothermal methods at 110 °C for pH 4, 7, 9, and 13. The surface morphology of the photocatalysts was examined by FE-SEM-EDS (Figs. 5 and 6). In Table 2, it was found that with the increase of hydrothermal temperature range from 110 to 260 °C, a gradual change in the crystal phase of the reflection peaks took place, which indicated a formation in the crystal phase from $\text{BiOCl}/\text{BiOBr}$ (or BiOCl) to $\alpha\text{-Bi}_2\text{O}_3$ at different reaction temperature. The FE-SEM image showed that the morphology of the bismuth oxybromochloride samples obtained with $\text{KCl}/\text{KBr}=1/2$ molar ratio at different reaction temperature turned from flower-like crystals to small plates, micro-cluster and irregular sheets and then became larger corner crystals (Fig. 5). Fig. 6 shows the morphology of the sample obtained with $\text{KCl}/\text{KBr}=2$ molar ratio at different pH values turning from irregular sheets to thin plates and thin sheets and then becoming super thin sheets

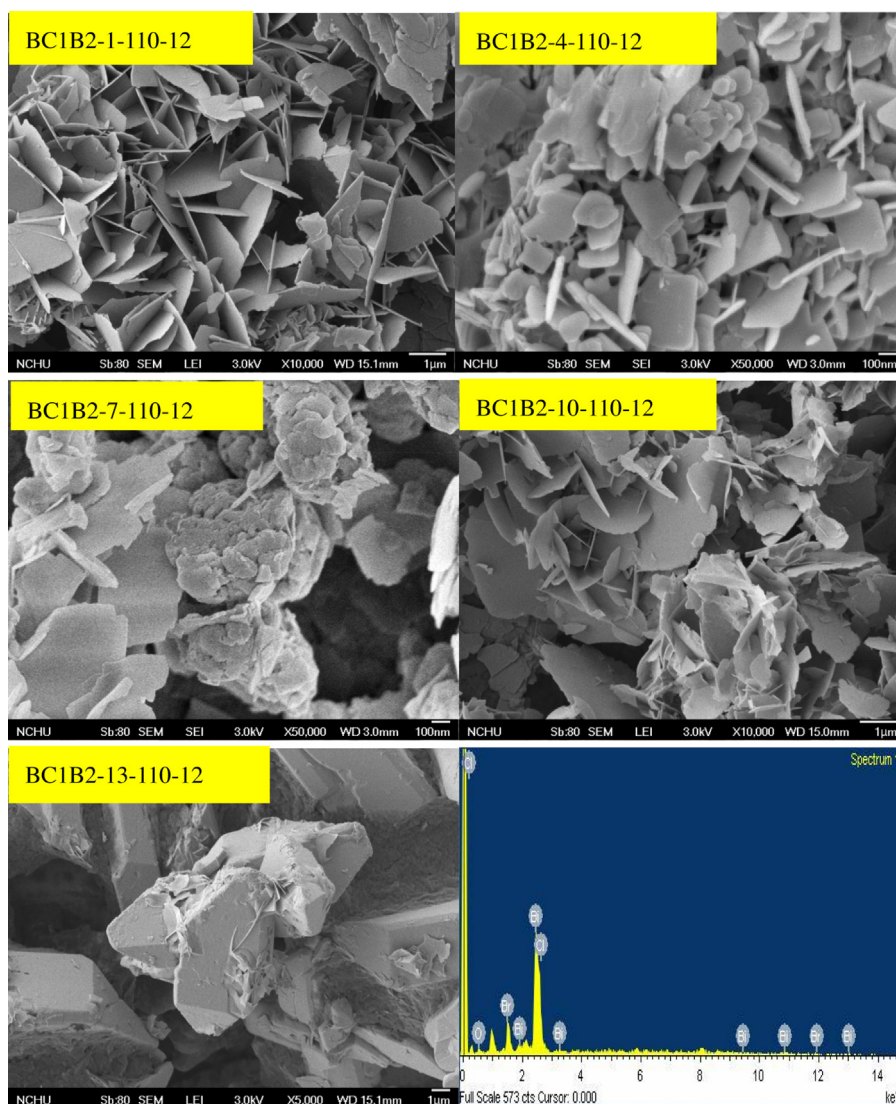


Fig. 5. SEM images of $\text{BiO}_x\text{Cl}_y/\text{BiO}_m\text{Br}_n$ prepared by the hydrothermal autoclave method at different pH values.

Table 3

Physical and chemical properties of $\text{BiO}_x\text{Cl}_y/\text{BiO}_m\text{Br}_n$.

Catalyst code	EDS of atomic ratio (%)				XPS of atomic ratio (%)				E_g (eV)
	Bi	O	Cl	Br	Bi	O	Cl	Br	
BC1B2-1-110-12	33.29	40.91	19.03	6.77	40.6	31.5	15.4	12.4	2.76
BC1B2-4-110-12	34.82	47.52	12.22	5.44	48.2	34.7	9.0	8.1	2.73
BC1B2-7-110-12	30.90	57.63	6.10	5.37	55.5	33.8	5.7	5.0	2.15
BC1B2-10-110-12	29.12	64.13	4.71	2.04	47.0	45.4	3.9	3.6	2.18
BC1B2-13-110-12	30.8	66.47	2.17	0.56	62.8	35.7	0.9	0.6	2.54
BC2B1-1-110-12	28.96	45.68	20.67	4.70	41.7	30.1	20.6	7.7	2.82
BC2B1-4-110-12	33.48	46.64	16.12	3.76	44.8	31.2	18.3	5.7	2.87
BC2B1-7-110-12	33.73	51.42	14.52	2.32	45.9	38.7	13.0	2.3	2.76
BC2B1-10-110-12	44.00	47.34	7.66	1.00	44.7	45.1	8.7	1.5	2.15
BC2B1-13-110-12	29.93	66.26	3.74	0.06	40.5	55.1	3.7	0.7	2.52
BC3-1-110-12	30.67	41.80	27.53	–	38.3	32.3	29.5	–	3.10
BB3-1-110-12	28.54	45.45	–	26.00	59.5	22.0	–	18.5	2.61

between pH=1 and pH=14. These samples displayed irregular nanoplates and nanosheet shapes with a lateral size of several decade micrometers and a thickness between 5 and 50 nm. Sample BC1B2-13-110-12 exhibited a rod-like irregular shape with a lateral size of several decade micrometers. From Table 3, the EDS results showed that the main elements of these samples were bismuth, chloride, bromine, and oxygen under different pH

values. The Cl (or Br) atomic ratios (%) of the samples were within the range 20.67–2.17 (or 6.77–0.06), which corresponded to BiOCl , $\text{Bi}_4\text{O}_5\text{Cl}_2$, $\text{Bi}_{24}\text{O}_{31}\text{Cl}_{10}$, $\text{Bi}_3\text{O}_4\text{Cl}$, $\text{Bi}_5\text{O}_7\text{Cl}$, $\text{Bi}_{12}\text{O}_{17}\text{Cl}_2$ (or BiOBr , $\text{Bi}_4\text{O}_5\text{Br}_2$, $\text{Bi}_{24}\text{O}_{31}\text{Br}_{10}$, $\text{Bi}_3\text{O}_4\text{Br}$, $\text{Bi}_5\text{O}_7\text{Br}$, $\text{Bi}_{12}\text{O}_{17}\text{Br}_2$), Bi_2O_3 and their mixture phase, compared to the stoichiometric ratio (Bi: Br (or Cl)=1, 2, 2.4, 3, 5, 6), and could be selectively prepared through a facile solution-based hydrothermal method. The possible

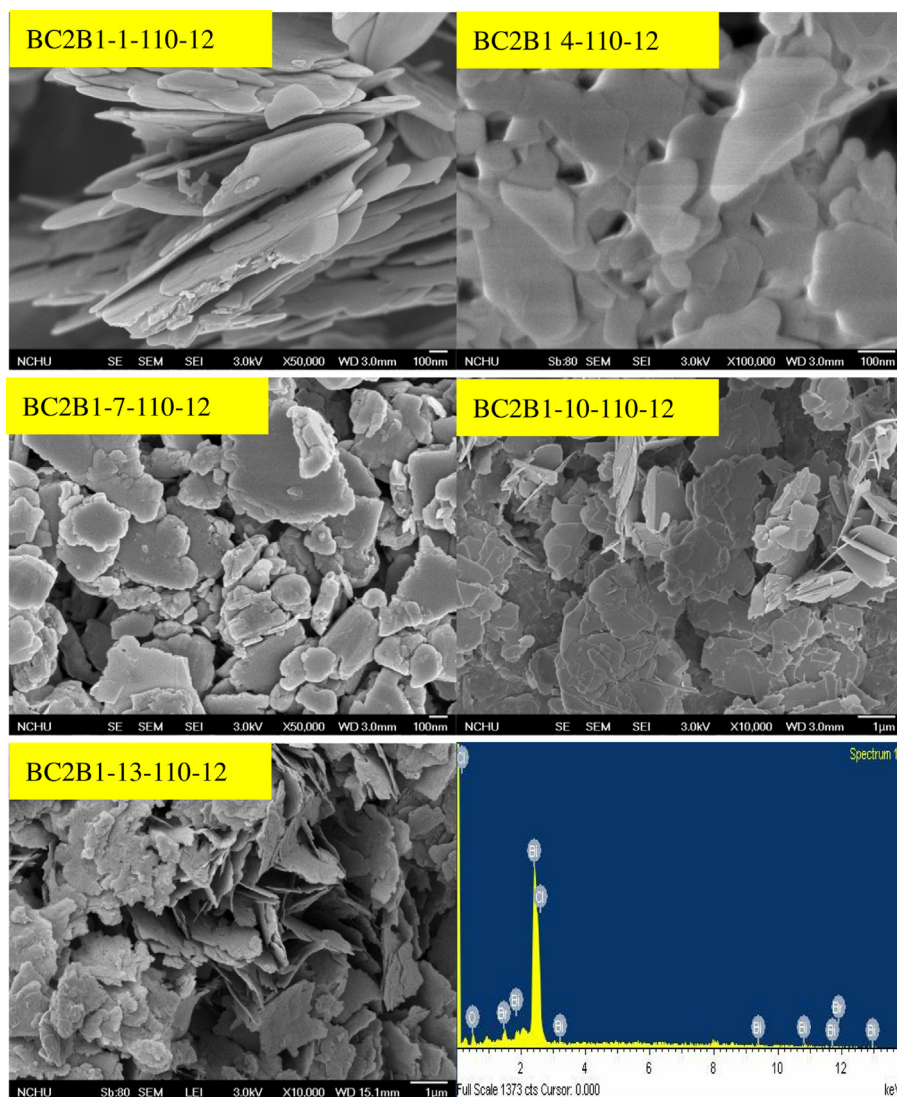


Fig. 6. SEM images of $\text{BiO}_x\text{Cl}_y/\text{BiO}_m\text{Br}_n$ prepared by the hydrothermal autoclave method at different pH values. (Molar ratio $\text{KCl}/\text{KBr} = 2$).

processes for the formation of bismuth oxychlorides and bismuth oxybromides were described as Eqs. (1)–(18). By controlling the pH and temperature of the reaction, different compositions of bismuth oxybromochloride were obtained.

Figs. 7–9 display that BC1B2-4-160-12, B1C2-7-160-12, and BC1B2-10-160-12 are composed of sheets or plates with different sizes, consistent with the TEM observation. In addition, the EDS spectrum showed the sample including Bi, O, Cl and Br elements. The HRTEM image revealed that two sets of different lattice images were found with the d spacing of 0.272 and 0.283 nm, corresponding to the (110) plane of BiOCl and the (012) plane of BiOBr (Fig. 7), 0.208 and 0.289 nm, corresponding to the (318) plane of $\text{Bi}_{24}\text{O}_{31}\text{Cl}_{10}$ and the (113) plane of $\text{Bi}_3\text{O}_4\text{Br}$ (Fig. 8), 0.200 and 0.289 nm, and corresponding to the (022) plane of $\text{Bi}_3\text{O}_4\text{Cl}$ and the (214) plane of $\text{Bi}_{24}\text{O}_{31}\text{Br}_{10}$ (Fig. 9), respectively, which was in good accordance with the results of the XRD patterns. The results suggested that the $\text{BiOCl}/\text{BiOBr}$, $\text{Bi}_{24}\text{O}_{31}\text{Cl}_{10}/\text{Bi}_3\text{O}_4\text{Br}$, and $\text{Bi}_3\text{O}_4\text{Cl}/\text{Bi}_{24}\text{O}_{31}\text{Br}_{10}$ heterojunctions have been formed in the composites, which would favor the separation of photoinduced carriers and thus acquire high photocatalytic activities. The EDS results showed that the main elements of these samples were bismuth, chlorine, bromine, and oxygen. The Cl (or Br) atomic ratio (%) of the samples was within the range 8.38–6.83 (or 18.52–6.53),

corresponding to different $\text{BiOCl}/\text{BiOBr}$, $\text{Bi}_{24}\text{O}_{31}\text{Cl}_{10}/\text{Bi}_3\text{O}_4\text{Br}$, and $\text{Bi}_3\text{O}_4\text{Cl}/\text{Bi}_{24}\text{O}_{31}\text{Br}_{10}$ heterojunctions.

3.1.3. XPS analysis

XPS was employed to examine the purity of the prepared $\text{BiO}_x\text{Cl}_y/\text{BiO}_m\text{Br}_n$ products, and the spectra are shown in Fig. 10 and Fig. S7. According to Fig. 10(a), the observation of transition peaks involving the Bi 4f, Cl 2p, Br 3d, O 1s, and C 1s orbitals revealed that the catalysts were constituted by the elements of Bi, O, Cl, Br, and C. Fig. 10 shows the total survey spectra of the Bi 4f, Cl 2p, Br 3d, and O 1s XPS of the five $\text{BiO}_x\text{Cl}_y/\text{BiO}_m\text{Br}_n$ samples. The characteristic binding energy value of 158.4–160.1 eV for $\text{Bi } 4f_{7/2}$ (Fig. 10(b)) revealed a trivalent oxidation state for bismuth. An additional spin–orbit doublet with binding energy of 156.2–159.3 eV for $\text{Bi } 4f_{7/2}$ was also observed in all samples, suggesting that certain parts of bismuth existed in the (+3–x) valence state. This indicated that the trivalent bismuth partially reduced to the lower valence state by the hydrothermal autoclave method. A similar chemical shift of approximately 2.2–2.6 eV for $\text{Bi } 4f_{7/2}$ was also observed by Jovalekic et al. [32] and Chen et al. [15,16]. They concluded that $\text{Bi}^{(+3-x)}$ formal oxidation state could most probably attribute to the substoichiometric forms of Bi within the Bi_2O_2 layer, and the formation of the low oxidation state resulted in oxygen vacancy in the

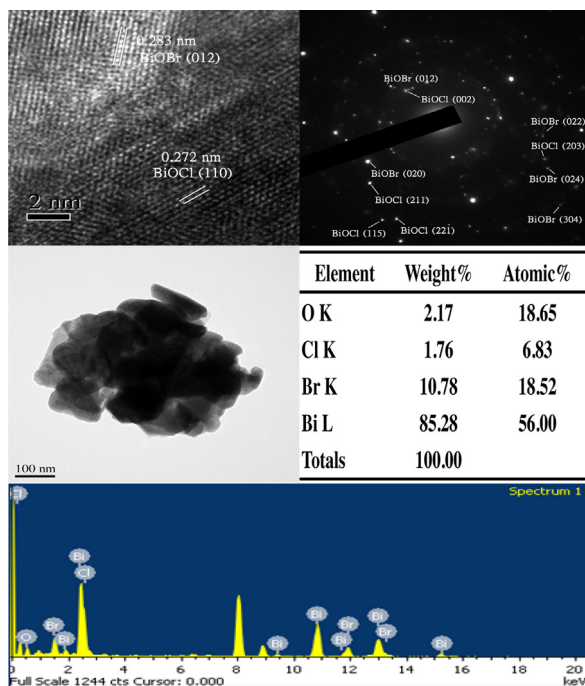


Fig. 7. FE-TEM images and EDS of BC1B2-4-160-12 sample by the hydrothermal autoclave method.

crystal lattice. However, it was assumed that $\text{Bi}^{(+3-x)}$ formal oxidation state could most likely attribute to the substoichiometric forms of Bi at the outer site of the particles, and the formation of the low oxidation state resulted in oxygen vacancy in the crystal surface. Fig. 10(c) shows the high-resolution XPS spectra for the O 1s region, which can be fitted into two peaks. The main peak at 529.8 eV was attributed to the Bi O bonds in $(\text{Bi}_2\text{O}_2)^{2+}$ slabs of BiOX layered structure, and the peak at 531.9 eV was assigned to the hydroxyl groups on the surface [27]. From Fig. 10(d), the binding energy of 197.2–198.1 eV and 199.0–199.6 eV was referred to the Cl 2p_{3/2} and 2p_{1/2} respectively which could be assigned to Cl at the monovalent oxidation state. The binding energy of 67.9–68.5 eV and 68.8–69.4 eV was referred to Br 3d_{5/2} and 3d_{3/2} respectively which could be assigned to Br at the monovalent oxidation state (Fig. 10(e)). In the BC1B2-13-110-12 and Bi₂O₃ samples, only two strong peaks centered at 163.9 and 158.2 eV could attribute to Bi 4f_{5/2} and Bi 4f_{7/2}, demonstrating that the main chemical states of the bismuth element in the samples were trivalent. The characteristic binding energy of 158.2 eV for Bi 4f_{7/2} revealed a trivalent oxidation state for Bi³⁺–O bonding. Two additional spin–orbit doublets with the binding energy of 158.8 and 159.2 eV for Bi 4f_{7/2} were also observed in all samples, suggesting that certain parts of bismuth existed in the Bi–Br and Bi–Cl bonding [33]. The XPS result revealed that the possible processes for the formation of bismuth oxybromides were described as Eqs. (1)–(18), which were consistent with previous results by XRD and TEM analyses. From Table 3, the results showed that the main elements of these samples were bismuth, chlorine, bromine, and oxygen. The Cl (or Br) atomic ratio (%) of the samples was within the range 24.6–0.9 (or 12.4–0.6), corresponding to different Bi_xCl_y/BiO_mBr_n heterojunctions.

3.1.4. Optical absorption properties

UV–vis diffuse reflectance spectra of different catalysts are shown in Fig. 11(a). It could be observed that BiO_xCl_y absorbed visible light slightly while the absorption edge of BiO_mBr_n extended nearly to the whole spectra of visible light. Moreover, the absorption edges of BiO_xCl_y/BiO_mBr_n composites had a monotonic red shift response of BiO_mBr_n. Based on their absorption spectra, E_g of

Table 4

Specific BET surface areas and pore parameters of the as-prepared BiO_xCl_y/BiO_mBr_n samples.

Catalyst code	BET (m ² /g)	Pore size (Å)	Pore volume (cm ³ /g)
BC1B2-1-110-12	5.51	441.85	0.065
BC1B2-4-110-12	12.11	347.45	0.123
BC1B2-7-110-12	7.90	366.65	0.079
BC1B2-10-110-12	10.05	447.97	0.122
BC1B2-13-110-12	0.020	1061.75	0.009
BC2B1-1-110-12	7.69	–	–
BC2B1-4-110-12	12.93	–	–
BC2B1-7-110-12	5.63	–	–
BC2B1-10-110-12	8.97	–	–
BC2B1-13-110-12	6.39	–	–
BC3-1-110-12	5.89	577.07	0.066
BB3-1-110-12	4.97	401.90	0.053

semiconductors could be calculated from $\alpha h\nu = A(h\nu - E_g)^{n/2}$ equation [34]. Among them, n was determined by the type of optical transition of a semiconductor ($n = 4$ for indirect transition and $n = 1$ for direct transition). The values of n for BiOCl and BiOBr were 4 and 4 respectively [35]. E_g of BiO_xCl_y/BiO_mBr_n was determined from a plot of $(\alpha h\nu)^{1/2}$ vs energy ($h\nu$) in Fig. 11(b) and elicited to be 2.15–2.87 eV in Table 3. The difference of band gap energy in the as-prepared BiO_xCl_y/BiO_mBr_n could be ascribed to their individual composition with various characteristics. Compared to BiOCl and BiOBr, BiO_xCl_y/BiO_mBr_n exhibited pronounced light absorbance abilities at $\lambda > 400$ nm, suggesting their potential photocatalytic activity under visible light. The steep shape and strong absorption in the visible region ascribed the visible light absorption to the intrinsic band gap transition between the valence band and the conduction band, rather than the transition from the impurity levels [36].

3.1.5. Specific surface areas and pore structure

Fig. 12(a) shows the nitrogen adsorption–desorption isotherm curves of BiO_xCl_y/BiO_mBr_n samples in different pH values. The isotherm of all samples was close to Type IV (Brunauer–Deming–Deming–Teller, BDDT, classification) with a hysteresis loop at highly relative pressure between 0.6 and 1.0 [33]. From Fig. 12(b), the shape of the hysteresis loop was close to Type H3, suggesting the existence of slit-like pores generally formed by the aggregation of plate-like particles, which was consistent with the self-assembled nanoplate-like morphology of samples [33]. This result was consistent with FE-SEM that the self-assembled nanosheets or nanoplates resulted in the formation of 3D hierarchical architecture. Fig. S8 shows the corresponding pore-size distribution (PSD) of BiO_xCl_y/BiO_mBr_n samples. As could be seen that for the BiO_xCl_y/BiO_mBr_n samples, PSD curves were tri-modal with small mesopore (2.1–2.2 nm), medium mesopore (10–50 nm), and large macropore (50–290 nm). As the nanosheets did not contain pores (Figs. 5 and 6), the smaller mesopores in the range 2.1–2.2 nm might reflect the porosity within nanosheets. The larger mesopores in the range 10.0–50 nm might be ascribed to the pores formed between stacked nanosheets. The macropores in the range 50–290 nm might be ascribed to the pores formed between flower-like nanosheets. Such self-organized porous architecture might be extremely useful in photocatalysis because they provided efficient transport pathways for the reactant and product molecules [27,37]. The pore parameters of BiO_xCl_y/BiO_mBr_n samples are summarized in Table 4.

In Table 4, BET of BiO_xCl_y/BiO_mBr_n was about 0.02–12.93 m²/g, which was lower than that of P25-TiO₂ with BET of 35.4 m²/g due to the increased particle size. The pore volume and size of composite sample distributed to 0.009–0.123 cm³/g, compared to pure BiOCl (0.066 cm³/g) and BiOBr (0.053 cm³/g). A greater specific surface

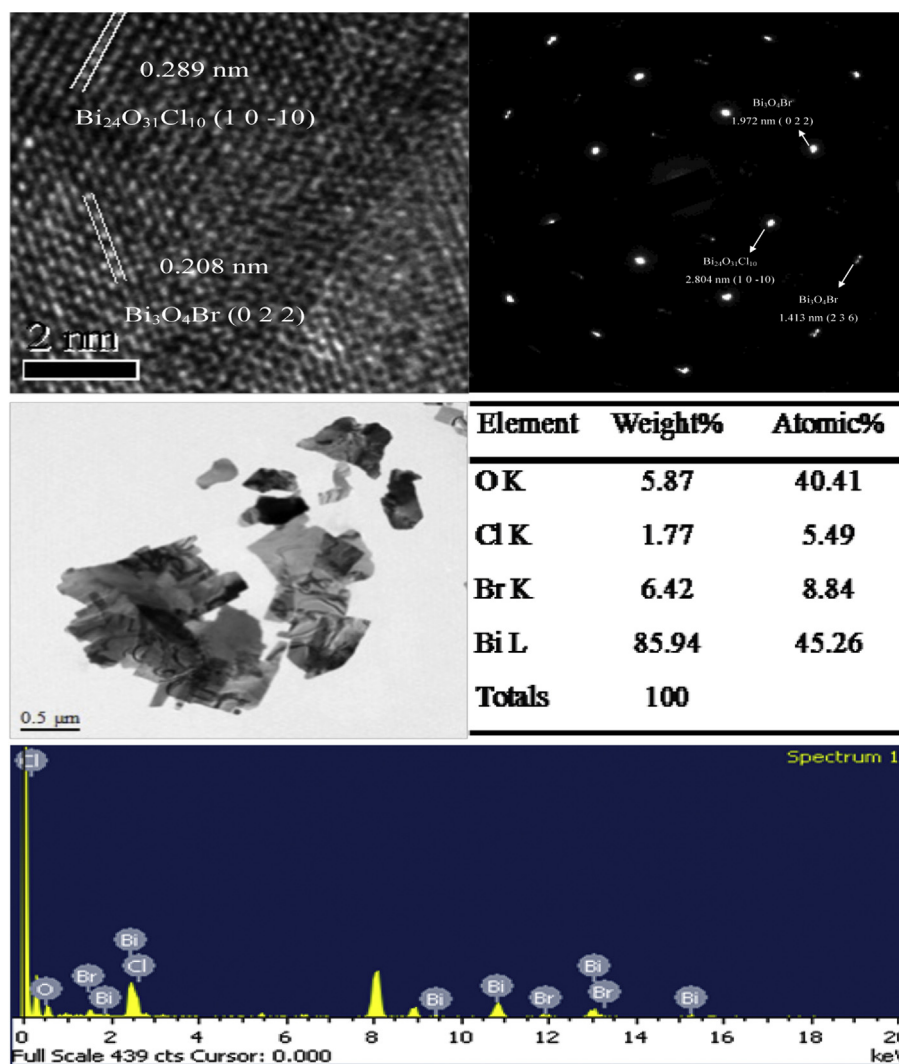


Fig. 8. FE-TEM images and EDS of BC1B2-7-160-12 sample by the hydrothermal autoclave method.

area and pore volume of photocatalyst could supply more surface active sites and make reactants transport easier, leading to an enhancement of the photocatalytic performance [38]. BC1B2-10-110-12 and BC2B1-10-110-12 have larger BET and the pore volume. Thus, the large BET and pore volume of $\text{BiO}_x\text{Cl}_y/\text{BiO}_m\text{Br}_n$ composites might play a role in enhancing the photocatalytic activity. These nanosheet and nanoplate structures could provide efficient transport paths for reactants and more active sites for the photocatalytic reaction. The structures were also favorable to efficient photoenergy harvesting and introducing the separation of electron-hole pairs, thus promoting the photocatalytic activity.

3.2. Photocatalytic activity

The photocatalytic performance of $\text{BiO}_x\text{Cl}_y/\text{BiO}_m\text{Br}_n$ catalysts was evaluated by degrading CV under visible light irradiation with 0.5 g/L of catalyst added. The degradation efficiency as a function of reaction time is illustrated in Fig. 13. The removal efficiency was enhanced significantly in the presence of $\text{BiO}_x\text{Cl}_y/\text{BiO}_m\text{Br}_n$ catalysts. After 48 h irradiation, $\text{BiO}_x\text{Cl}_y/\text{BiO}_m\text{Br}_n$ showed superior photocatalytic performance, with CV removal efficiency up to 99%. To further understand the reaction kinetics of CV degradation, the apparent pseudo-first-order model [39] expressed by $\ln(C_0/C) = k_{\text{app}}t$ equation was applied to the experiments, where k_{app} was the apparent pseudo-first-order rate constant (h^{-1}), C the

CV concentration in aqueous solution at time t (mg/L), and C_0 the initial CV concentration (mg/L). Via the first-order linear fit from the data of Fig. 13 shown in Table 5, k_{app} of BC1B2-10-110-12 was obtained at the maximal degradation rate of $7.64 \times 10^{-2} \text{ h}^{-1}$, greatly higher than the other heterojunctions. The result showed that the $\text{Bi}_3\text{O}_4\text{Cl}/\text{Bi}_{24}\text{O}_{31}\text{Br}_{10}$ heterojunction composite was a much more effective photocatalyst than the others. However, this result displayed that BC2B1-4-110-12 with the highest BET did not represent the highest photocatalytic activity among the samples, which suggested that the changes in the photocatalytic activity result from the $\text{BiO}_x\text{Cl}_y/\text{BiO}_m\text{Br}_n$ heterojunction rather than BET. Therefore, the $\text{Bi}_3\text{O}_4\text{Cl}/\text{Bi}_{24}\text{O}_{31}\text{Br}_{10}$ heterostructure showed the best photocatalytic activity. From Table 4, BC1B2-10-110-12 had larger BET and the pore volume. Thus, large BET and pore volume of $\text{BiO}_x\text{Cl}_y/\text{BiO}_m\text{Br}_n$ composites might play the roles to enhance the photocatalytic activity. In the absence of catalysts, CV could not be degraded under visible light irradiation. The superior photocatalytic ability of $\text{BiO}_x\text{Cl}_y/\text{BiO}_m\text{Br}_n$ might be ascribed to its efficient utilization of visible light and the high separation efficiency of the electron-hole pairs with its heterojunctions.

3.3. Mechanism

Generally speaking, three possible reaction mechanisms were suspected to be involved in dye photodegradation by a

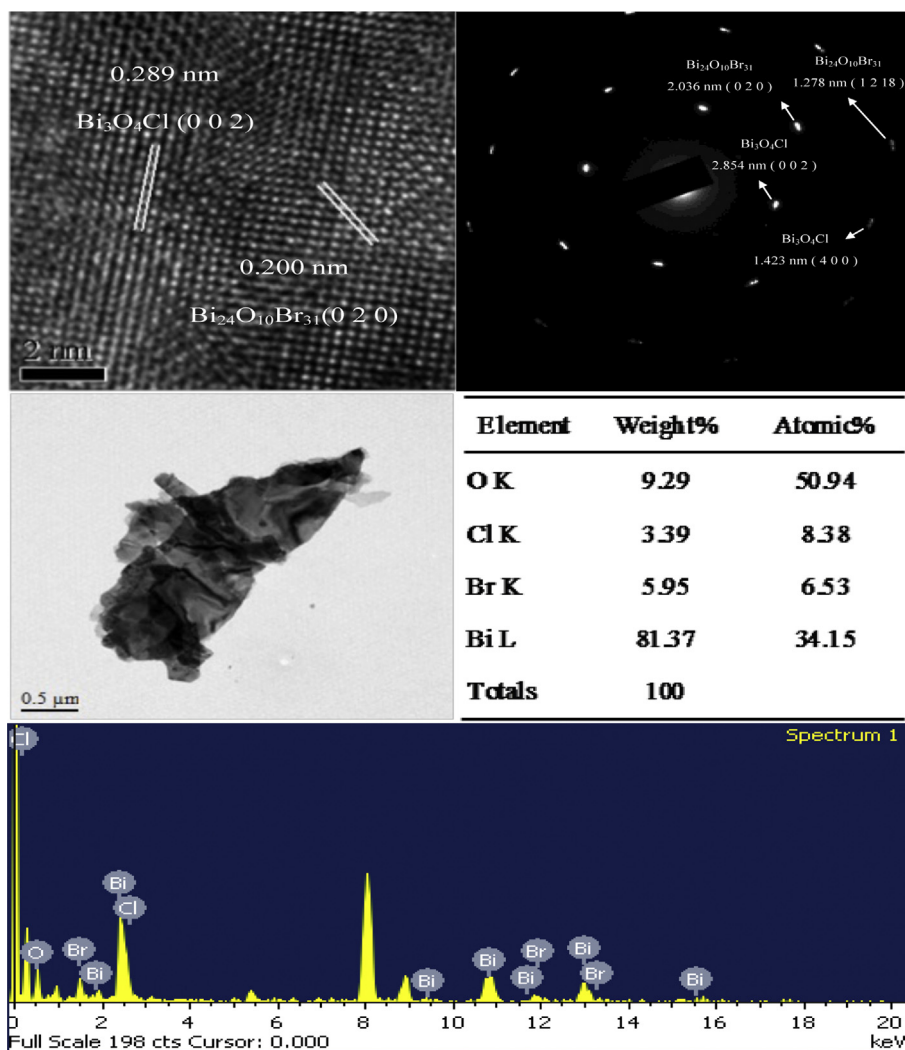


Fig. 9. FE-TEM images and EDS of BC1B2-10-160-12 sample by the hydrothermal autoclave method.

Table 5

The pseudo-first-order rate constants for the degradation of CV with $\text{BiO}_x\text{Cl}_y/\text{BiO}_m\text{Br}_n$ photocatalysts under visible light irradiation.

pH	Temp (°C)		160		210		260		
	110		k (h ⁻¹)	R ²	k (h ⁻¹)	R ²	k (h ⁻¹)	R ²	
BC1B2									
1	0.0555	0.9867	0.0385	0.9619	0.0384	0.9638	0.0605	0.9516	
4	0.0509	0.9803	0.0489	0.9660	0.0377	0.9571	0.0587	0.9556	
7	0.0578	0.9739	0.0511	0.9508	0.0423	0.9537	0.0723	0.9642	
10	0.0764	0.9574	0.0691	0.9512	0.0575	0.9563	0.0554	0.9531	
13	0.0319	0.9539	0.0191	0.9656	0.0140	0.9504	0.0247	0.9536	
BC2B1									
1	0.0364	0.9741	0.0375	0.9564	0.0337	0.9588	0.0174	0.9839	
4	0.0548	0.9654	0.0536	0.9803	0.0499	0.9967	0.0490	0.9943	
7	0.0392	0.9846	0.0287	0.9945	0.0631	0.9778	0.0585	0.9533	
10	0.0678	0.9697	0.0536	0.9666	0.0369	0.9518	0.0391	0.9543	
13	0.0123	0.9621	0.0615	0.9576	0.0128	0.9738	0.0304	0.9634	
BiOCl		BiOBr							
k (h ⁻¹)	R ²	k (h ⁻¹)	R ²						
0.0229	0.9728	0.0375	0.9660						

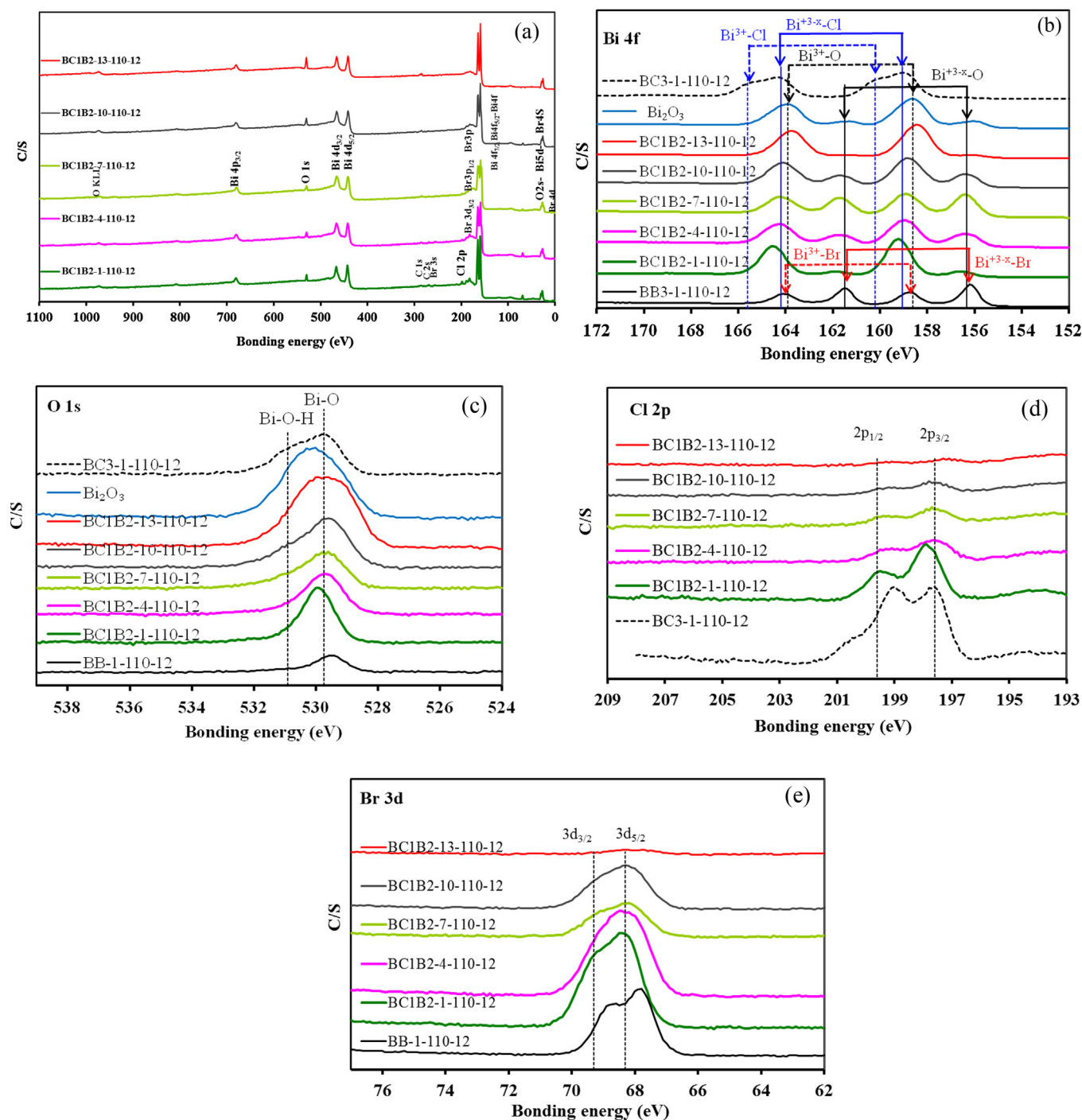


Fig. 10. High resolution XPS spectra of as-prepared $\text{BiO}_x\text{Cl}_y/\text{BiO}_m\text{Br}_n$ samples under different pH values. (a) Total survey; (b) Bi 4f; (c) O 1s; (d) Cl 2p; (e) Br 3d. (Molar ratio $\text{KCl}/\text{KBr} = 1/2$).

semiconductor, namely photolysis process, dye photosensitization process, and photocatalytic process [40]. For the photolysis process, a photoinduced electron on the induced dye directly reacted with O_2 to produce a singlet oxygen atom that could work as an oxidant for the pure dye's photolysis [40,41]. In this experiment, CV degradation by the photolysis process upon visible light in the blank experiment was not observable. This meant that CV was a kind of structure-stable dye, thus, the CV decomposition by the photolysis mechanism was negligible.

For a dye photosensitization process, the energy of irradiation light could stimulate the dye to form photoinduced electrons

which transferred to the conduction band of the catalyst absorbing the dye and subsequently reacted with O_2 to generate $\text{O}_2^{\bullet-}$ oxidant [35,40,42]. As previous studies shown, the properties of the dye, such as the structural stability of the dye, the adsorbability of the dye on catalyst surface, and the absorbance of the dye, were responsible for a dye photosensitization mechanism. In this study, slight changes in the CV concentration over different samples could be detected in 30 min of dark adsorption experiment before the photocatalytic reactions. The slight CV adsorptions on the catalyst benefited the transfer of charge carriers between the dye and the catalyst surfaces in the dye photosensitization

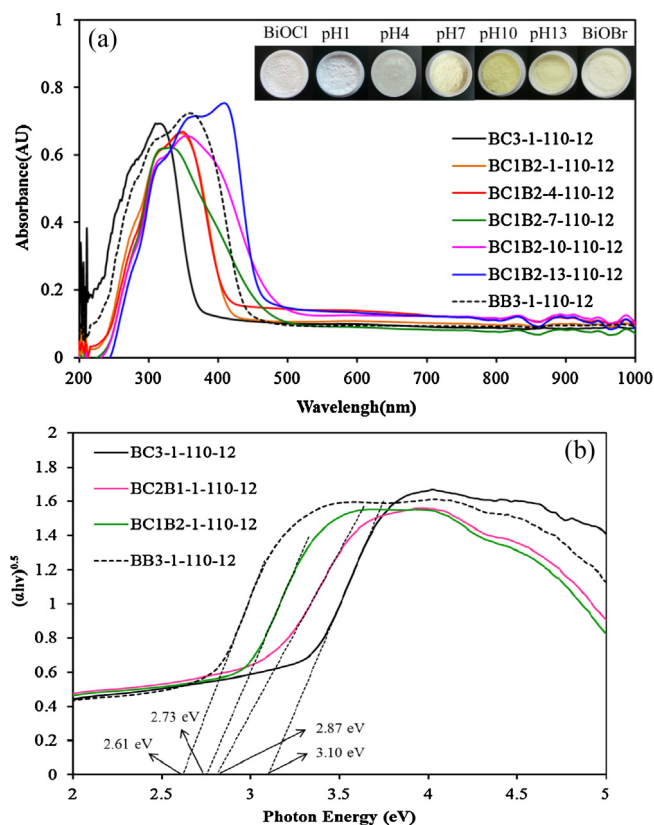


Fig. 11. UV-vis absorption spectra of as-prepared $\text{BiO}_x\text{Cl}_y/\text{BiO}_m\text{Br}_n$ samples under different (a) pH values and (b) molar ratio.

process. Presumably the photosensitization processes taking place over $\text{BiO}_x\text{Cl}_y/\text{BiO}_m\text{Br}_n$, that is to say, the photosensitization mechanism in the CV decomposition is also not neglectable as well as the photolysis mechanism.

As is known, the photocatalysts were excited to generate electron-hole pairs directly after the illumination in the photocatalytic process. Moreover, the photocatalytic efficiency mainly depended on the recombination rate or lifetime of the photogenerated electron-hole pairs. The faster recombination occurred, the less time was for the chemical reactions. Therefore, cathodoluminescence (CL) spectrum was utilized for investigating the recombination rate of the photogenerated electron-hole pairs [43]. To investigate the separation capacity of photogenerated carriers in heterostructures, CL spectra of BiOCl , BiOBr , and $\text{BiO}_x\text{Cl}_y/\text{BiO}_m\text{Br}_n$ were measured and the results were given in Fig. 14. A strong emission peak around 2.01 eV appeared on BiOCl (BC3-1-110-12) and BiOBr (BB3-1-110-12), which might be derived from the direct electron-hole recombination of band transition. However, the characteristic emission peak around 2.01 eV nearly disappeared on the $\text{BiO}_x\text{Cl}_y/\text{BiO}_m\text{Br}_n$ heterostructure, indicating that the recombination of photogenerated charge carriers was inhibited greatly. The efficient charge separation could increase the lifetime of charge carriers and enhance the efficiency of interfacial charge transfer to adsorbed substrates and then improve the photocatalytic activity.

In Fig. 14, the lowest relative CL intensity of BC2B1-13-110-12 heterostructure suggested that it had the lowest recombination rate of electron-hole pairs, which resulted in the highest photocatalytic activity of BC1B2-10-110-12, as shown in Fig. 13 and Table 5. Therefore, it was believed that the CV degradation was initiated not only by a photocatalytic process but also by a photosensitization process.

As is known, various primary reactive species, such as hydroxyl radical HO^\bullet , photogenerated hole h^+ , superoxide radical $\text{O}_2^{\bullet-}$ and

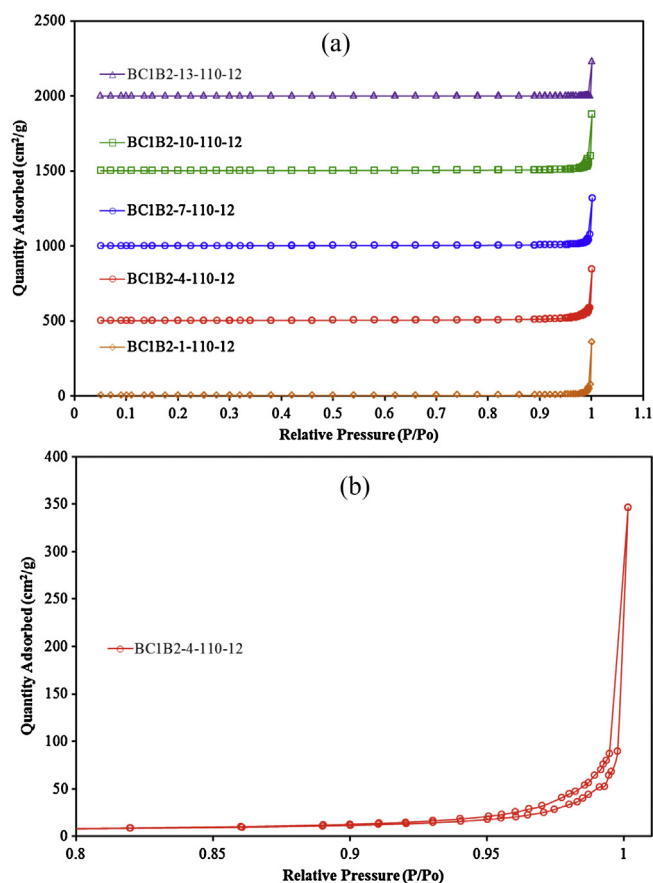


Fig. 12. N_2 adsorption-desorption isotherm distribution curves for (a) as-prepared $\text{BiO}_x\text{Cl}_y/\text{BiO}_m\text{Br}_n$ samples under different pH values and (b) enlarged view of BC1B2-4-110-12.

singlet oxygen $^1\text{O}_2$, could be formed during the photocatalytic degradation process in the UV-vis/semiconductor system [44]. Cao et al. investigated that hydroxyl radicals and direct holes were the primary reactive species in the methyl orange degradation by BiOI/BiOBr spheres under visible light irradiation [35]. Shenawi-Khalil and his coworkers showed that Rhodamine-B photodegradation by $y\text{BiO}(\text{Cl}_x\text{Br}_{1-x}) - (1-y)$ bismuth oxide hydrate under visible light was dominated by $\text{O}_2^{\bullet-}$ and h^+ oxidation being the main active species [45]. Xiao's group revealed that high-efficiency visible light driven bisphenol-A removal with BiOI/BiOCl could attribute to effective separation and transfer of photoinduced charge carriers in BiOI/BiOCl with narrower band gap and more negative conduction band position, which favored the photogenerated holes [46]. Chen et al. proposed the pathway for generating active oxygen radicals ($^\bullet\text{OH}$) on the surface of $\text{Bi}_2\text{O}_2\text{CO}_3/\text{BiOI}$ for the degradation of Rhodamine-B, Methylene Blue, and Crystal Violet [47]. Sanaa et al. reported $^\bullet\text{OH}$ and h^+ being two main actives in the whole degradation process [48]. Wang et al. reported that $^\bullet\text{OH}$ radical was generated by multistep reduction $\text{O}_2^{\bullet-}$ [33]. The generation of $\text{O}_2^{\bullet-}$ could not only inhibit the recombination of photoinduced charge carriers, but also benefit the dechlorination of chlorinated phenol derivative. The hydroxyl radical HO^\bullet might only be generated via an $e^- \rightarrow \text{O}_2^{\bullet-} \rightarrow \text{H}_2\text{O}_2 \rightarrow ^\bullet\text{OH}$ route. Meanwhile, $^\bullet\text{OH}$ radical was generated by multistep reduction $\text{O}_2^{\bullet-}$ in the system. In a valence band of Bi^{3+} , holes formed by photoexcitation were regarded as Bi^{5+} [49]. The standard redox potential of $\text{Bi}^{\text{V}}/\text{Bi}^{\text{III}}$ was more negative than that of $\text{OH}^\bullet/\text{OH}^-$ [50]. Therefore, photogenerated holes on the surface of Bismuth Oxyhalides were not expected to react with $\text{OH}^-/\text{H}_2\text{O}$ to form $^\bullet\text{OH}$, suggesting that the decomposition of bisphenol-A [46] and Rhodamine [45] could attribute to

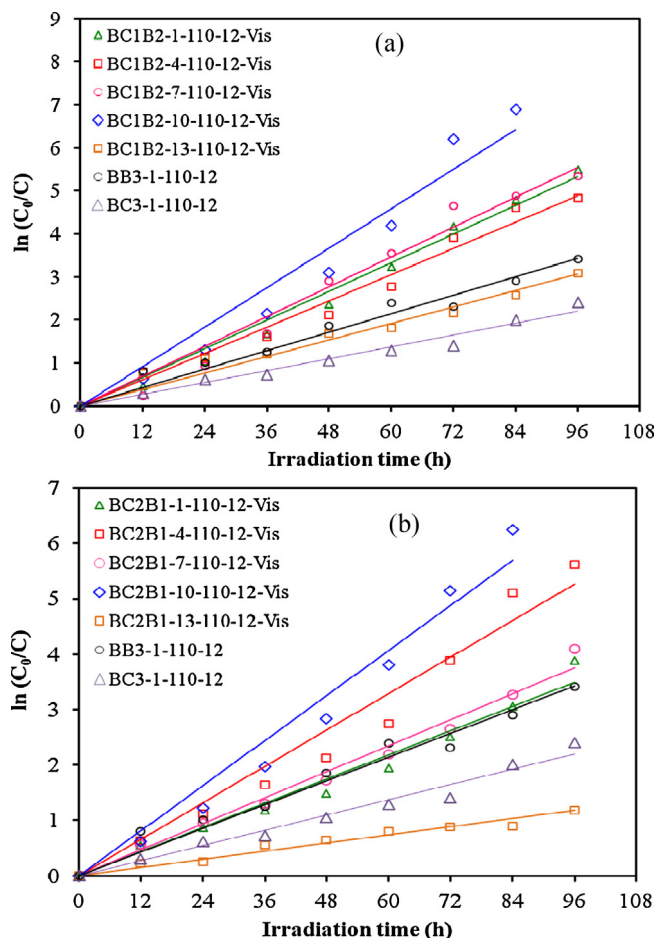


Fig. 13. Photodegradation of CV as a function of irradiation time over different $\text{BiO}_x\text{Cl}_y/\text{BiO}_m\text{Br}_n$ photocatalysts. Molar ratio KCl/KBr (a) 1/2 and (b) 2/1.

a direct reaction with the photogenerated holes or with superoxide radical (generated by the excited electron) or both species. Zhu et al. [51] reported that photocatalytic experiments in the presence of N_2 and the radical scavenger suggested $\cdot\text{OH}$ and $\text{O}_2^{\cdot-}$ being two main actives in the whole degradation process. According to previous studies [19], the dominant active oxygen species generated in direct oxidation and photocatalytic reactions were $^1\text{O}_2$ and $\cdot\text{OH}$ radical, respectively. Besides, in this visible light-induced semiconductor system, hydroxylated compounds were also identified for the photocatalytic degradation of CV and ethyl violet [52]. On the basis of above results and discussion, it was proposed that the probability for the formation of $\cdot\text{OH}$ should be much lower than it for $\text{O}_2^{\cdot-}$. But, the $\cdot\text{OH}$ was an extremely strong, non-selective oxidant, which led to the partial or complete mineralization of several organic chemicals.

Chen et al. [12] reported that Pt-TiO₂ accumulated less negative species on catalyst surfaces, which deteriorated reaction rates, than pure TiO₂ did in an acidic environment. $\cdot\text{OH}$ radical was produced subsequently, as shown in Eqs. (19)–(24).

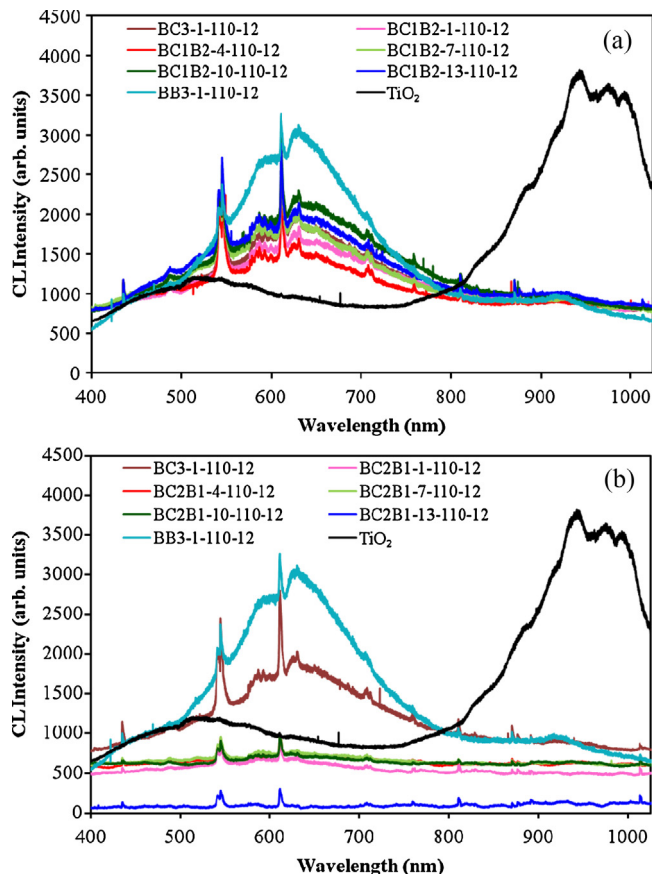
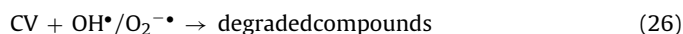
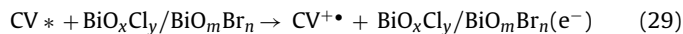


Fig. 14. Cathodoluminescence spectra of TiO₂, BiOCl, BiOBr, and $\text{BiO}_x\text{Cl}_y/\text{BiO}_m\text{Br}_n$. Molar ratio KCl/KBr (a) 1/2 and (b) 2/1.

These cycles continuously occurred when the system was exposed to the visible light irradiation. Finally, after several cycles of photo-oxidation, the degradation of CV by the formed oxidant species could be expressed by Eqs. (25)–(27):



It has been reported that dye exhibits a mechanism of dye sensitized degradation [51,53]. This photocatalytic degradation also attributed to the photodegradation of CV through the photocatalytic pathway of CV photosensitized $\text{BiO}_x\text{Cl}_y/\text{BiO}_m\text{Br}_n$. CV absorbing a visible photon was promoted to an excited electronic state CV^* , from which an electron could be transferred into the conduction band of $\text{BiO}_x\text{Cl}_y/\text{BiO}_m\text{Br}_n$:



Once the electron reached the $\text{BiO}_x\text{Cl}_y/\text{BiO}_m\text{Br}_n$ conduction band, it subsequently induced the generation of active oxygen species (Eqs. (30) and (19)–(22)), resulting in the degradation of CV. Clearly, apart from the photodegradation of CV through the pathway of $\text{BiO}_x\text{Cl}_y/\text{BiO}_m\text{Br}_n$ -mediated and photosensitized processes, there was another kind of photocatalytic pathway to account for the enhanced photocatalytic activity. Both the photocatalytic process and the photosensitized process would work concurrently, as shown in Fig. 15. $\cdot\text{OH}$ and $\text{O}_2^{\cdot-}$ were two main active species in the whole process.

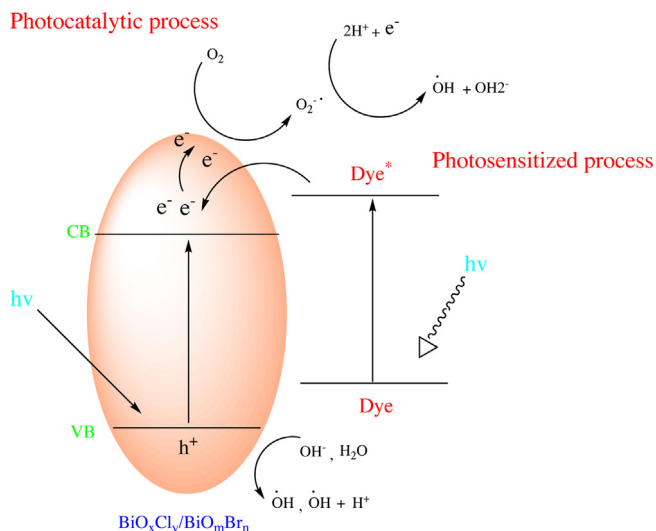


Fig. 15. The band structure diagram of $\text{BiO}_x\text{Cl}_y/\text{BiO}_m\text{Br}_n$ nanocomposites and the possible charge separation processes.

3.4. Photodegradation of CV

3.4.1. Separation and Identification of the intermediates

With visible irradiation, temporal variations occurring in the solution of CV dye during the degradation process being examined by HPLC coupled with a photodiode array detector and ESI mass spectrometry. Given the irradiation of CV up to 24 h at pH 4, the chromatograms were illustrated in Fig. 16 and recorded at 580, 350, and 300 nm, and nineteen intermediates were identified, with the retention time under 50 min. The CV dye and its related intermediates were denoted as species **A–J**, **a–f**, and α – γ . Except for the

initial CV dye (peak A), the peaks initially increased before subsequently decreasing, indicating the formation and transformation of the intermediates.

In Fig. S9 of Appendix, the maximum absorption of the spectral bands shifted from 588.1 nm (spectrum A) to 542.1 nm (spectrum J), from 373.6 nm (spectrum a) to 339.3 nm (spectrum f), and from 292.5 nm (spectrum α) to 278.2 nm (spectrum γ). The maximum adsorption in the visible and ultraviolet spectral region of each intermediate is depicted in Table 6. They were identified as **A–J**, **a–f**, and α – γ , respectively corresponding to the peaks A–J, a–f, and α – γ in Fig. 16. These shifts of the absorption band were presumed to result from the formation of a series of *N*-de-methylated intermediates. From these results, several families of intermediates could be distinguished.

The first family is marked in the chromatogram of Fig. 16(a) and illustrated in Fig. S9(a) for UV–vis absorption spectroscopy. The wavelength position of the major adsorption band of the intermediates of *N*-de-methylated CV dye moved toward the blue region, λ_{max} , **A** (CV), 588.1 nm; **B**, 581.2 nm; **C**, 574.2 nm; **D**, 578.8 nm; **E**, 566.2 nm; **F**, 571.4 nm; **G**, 562.3 nm; **H**, 566.5 nm; **I**, 554.3 nm; **J**, 542.1 nm. The *N*-de-methylation of the CV dye caused the wavelength shifts, depicted in Table 6, due to an attack by one of the active oxygen species on the *N,N*-dimethyl or *N*-methyl group. It was previously reported [12] that the CV dye was *N*-de-methylated in a stepwise manner (i.e., methyl groups were removed one by one as confirmed by the gradual peak wavelength shifts toward the blue region) and this was confirmed as shown in Table 6.

The second family is marked in the chromatogram of Fig. 16(b) and illustrated in Fig. S9(b) for UV–vis absorption spectroscopy. The destruction of CV yielded **a**, α , and their *N*-de-methylated products *N*-hydroxymethylated intermediates. The wavelength position of the major adsorption band of the *N*-de-methylation of the **a** and the *N*-hydroxymethylated intermediates of the *N*-de-methylated **a** species, produced by the cleavage of the CV chromophore ring structure, moved toward the blue region,

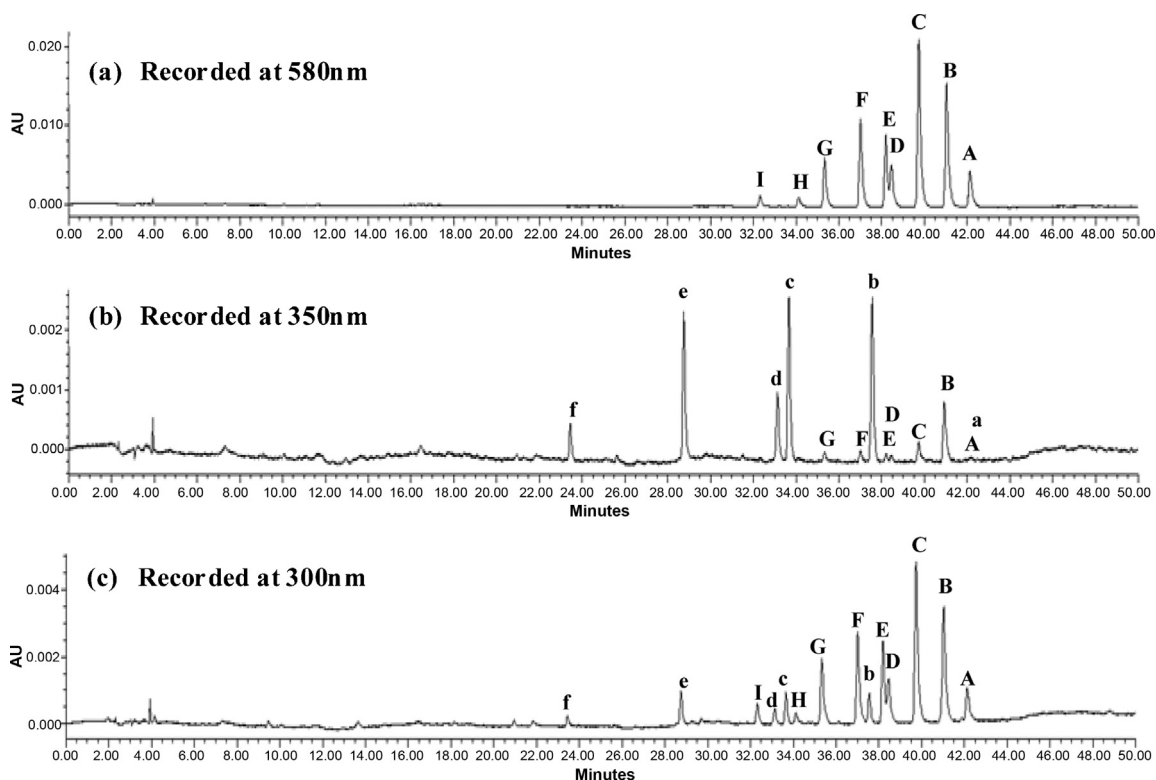


Fig. 16. HPLC chromatogram of the degraded intermediates at different irradiation intervals, recorded at (a) 580 nm, (b) 350 nm and (c) 300 nm.

Table 6
Summary of the CV photocatalytic degradation intermediates identified by the HPLC-PDA-ESI/MS.

HPLC peaks	De-methylation intermediates	ESI/MS molecular ions (<i>m/z</i>)	Adsorption maximum (nm)
A	<i>N, N, N', N', N'', N''</i> -hexamethyl-pararosaniline	372.40	588.1
B	<i>N, N</i> -dimethyl- <i>N', N'</i> -dimethyl- <i>N''</i> -methyl-pararosaniline	358.45	581.2
C	<i>N, N</i> -dimethyl- <i>N'</i> -methyl- <i>N''</i> -methyl-pararosaniline	344.35	574.2
D	<i>N, N</i> -dimethyl- <i>N', N'</i> -dimethyl-pararosaniline	344.35	578.8
E	<i>N</i> -methyl- <i>N'</i> -methyl- <i>N''</i> -methyl-pararosaniline	330.35	566.2
F	<i>N, N</i> -dimethyl- <i>N'</i> -methyl-pararosaniline	330.22	571.4
G	<i>N</i> -methyl- <i>N'</i> -methyl-pararosaniline	316.39	562.3
H	<i>N, N</i> -dimethyl-pararosaniline	316.34	566.5
I	<i>N</i> -methyl-pararosaniline	302.29	554.3
J	pararosaniline	288.17	542.1
a	4-(<i>N, N</i> -dimethylamino)-4'-(<i>N', N'</i> -dimethylamino)benzophenone	269.33	373.6
b	4-(<i>N, N</i> -dimethylamino)-4'-(<i>N'</i> -methylamino)benzophenone	255.28	366.0
c	4-(<i>N</i> -methylamino)-4'-(<i>N'</i> -methylamino)benzophenone	241.03	362.6
d	4-(<i>N, N</i> -dimethylamino)-4'-aminobenzophenone	241.22	362.6
e	4-(<i>N</i> -methylamino)-4'-aminobenzophenone	227.11	357.0
f	4,4'-bis-aminobenzophenone	213.27	339.3
α	4-(<i>N, N</i> -dimethylamino)phenol	138.20	292.5
β	4-(<i>N</i> -methylamino)phenol	121.05	288.9
γ	4-aminophenol	110.95	278.2

λ_{\max} , **a**, 373.6 nm; **b**, 366.0 nm; **c**, 362.6 nm; **d**, 362.6 nm; **e**, 357.0 nm; **f**, 339.3 nm. The proposed intermediate (**a**) was compared with a standard material of 4-(*N, N*-dimethylamino)-4'-(*N', N'*-dimethylamino)benzophenone. The retention time and the absorption spectra were identical.

The third family is marked in the chromatogram of Fig. 16(c) and illustrated in Fig. S9(c) for UV-vis absorption spectroscopy. The wavelength position of the major adsorption band of the *N*-de-methylation of the **α**, produced by the cleavage of the CV chromophore ring structure, moved toward the blue region, λ_{\max} , **α**, 292.5 nm; **β**, 288.9 nm; **γ**, 278.2 nm. The proposed intermediate (**γ**) was compared with the standard material of

4-aminobenzophenone. The retention time and the absorption spectra were identical.

The intermediates were further identified using the HPLC-ESI mass spectrometric method, and the relevant mass spectra were illustrated in Table 6. The molecular ion peaks appeared in the acid forms of the intermediates. The results of mass spectral analysis confirmed that the component **A** (CV), $m/z=372.40$, **B**, $m/z=358.23$; **C**, $m/z=344.35$; **D**, $m/z=344.23$; **E**, $m/z=330.17$; **F**, $m/z=330.22$; **G**, $m/z=316.17$; **H**, $m/z=316.12$; **I**, $m/z=302.12$; **J**, $m/z=288.12$; **a**, $m/z=269.28$; **b**, $m/z=255.23$; **c**, $m/z=241.05$; **d**, $m/z=241.27$; **e**, $m/z=227.37$; **f**, $m/z=213.30$; **α**, $m/z=138.08$, in liquid chromatogram.

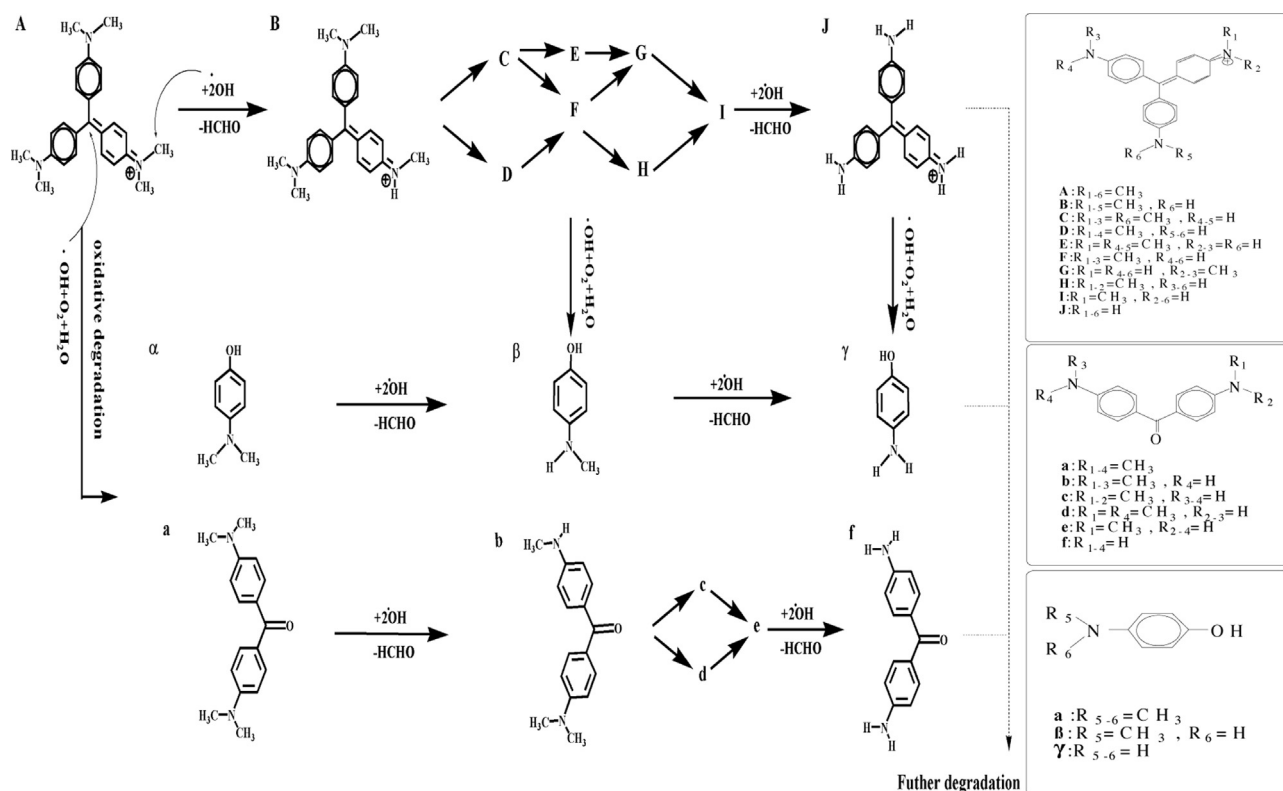


Fig. 17. Proposed photodegradation mechanism of the CV dye.

3.4.2. Photodegradation mechanisms of CV

In earlier reports [12], the *N*-de-alkylation processes were preceded by the formation of a nitrogen-centered radical while the oxidative degradation (destruction of dye chromophore structures) was preceded by the generation of a carbon-centered radical in the photocatalytic degradation of Triphenylmethane dye. On the basis of the above experimental results, the dye degradation mechanism was tentatively proposed, depicted in Fig. 17. The excited dye injected an electron into the conduction band of $\text{BiO}_x\text{Cl}_y/\text{BiO}_m\text{Br}_n$, where it was scavenged by O_2 to form $\text{O}_2^{\cdot-}$. De-methylation of CV dye occurred mostly through attack by the active species, which was a perfect nucleophilic reagent, on the *N*-methyl portion of CV. Further, $\text{O}_2^{\cdot-}$ subsequently reacted with H_2O to generate $\cdot\text{OH}$ radical and the other active radical. The probability for the formation of $\cdot\text{OH}$ should be much lower than that for $\text{O}_2^{\cdot-}$. $\cdot\text{OH}$ was an extremely strong, non-selective oxidant, which led to the partial or complete mineralization of several organic chemicals. All the above active radicals drove the photodegradation or mineralization of the dye molecule. Under visible light irradiation, all the intermediates identified in these two studied topics had the same result. There was no doubt that the major oxidant was $\cdot\text{OH}$ radical, not $\text{O}_2^{\cdot-}$.

During the initial period of CV dye photodegradation by $\text{BiO}_x\text{Cl}_y/\text{BiO}_m\text{Br}_n$, competitive reactions between *N*-de-methylation and oxidative degradation occurred based on the intermediates identified. The detailed mechanisms are illustrated in the Figs. S10–S11. The first pathway involved in a hydroxyl radical attack on the *N,N*-methylamino group of CV, resulting in a reactive cationic radical, the subsequent de-methylation and oxidation of which eventually yielded the first group intermediates. The results indicated that the *N*-de-methylation degradation of CV dye took place in a stepwise manner to yield mono-, di-, tri-, tetra-, penta-, hexa-*N*-de-methylated CV species during the process.

The second pathway involved in a hydroxyl radical attack on the central carbon atom of CV, yielding a reactive cationic radical, with a bond between the central carbon atom and the *N,N*-dimethylamino phenyl ring that was cleaved to give one set of intermediates **a** and **α**. In addition, these intermediates could further be attacked by hydroxyl radicals, giving a reactive cationic radical which was de-methylated, resulting in **f** and **γ**. The latter intermediates were further oxidized to form mineralization products.

4. Conclusions

The pH of a reaction is generally accepted to have great influence on determining the compositions and morphologies of the final products. Control experiments have been conducted to investigate the influence of pH on the hydrothermal reaction. The increased photocatalytic activities of $\text{BiO}_x\text{Cl}_y/\text{BiO}_m\text{Br}_n$ could be attributed to the formation of the heterojunction between BiO_xCl_y and BiO_mBr_n , which effectively suppresses the recombination of photoinduced electron–hole pairs. Both the photocatalytic process and the photosensitized process would work concurrently. $\cdot\text{OH}$ and $\text{O}_2^{\cdot-}$ are two main active species in the whole process. In the photocatalytic process and the photosensitized process, both *N*-de-methylation and conjugated structure of CV dye take place during the degradation process with $\text{BiO}_x\text{Cl}_y/\text{BiO}_m\text{Br}_n$ being the catalyst. The reaction mechanisms for Vis/ $\text{BiO}_x\text{Cl}_y/\text{BiO}_m\text{Br}_n$ proposed in this study should offer some insight for the future development of technology applications to the degradation of dyes.

Acknowledgment

This research was supported by the National Science Council of the Republic of China (NSC-101-2113-M-142-001-MY3).

Appendix A. Supplementary data

Supplementary data associated with this article can be found, in the online version, at <http://dx.doi.org/10.1016/j.molcata.2014.04.020>.

References

- [1] L. Young, J. Yu, *Water Res.* 31 (1997) 1187–1193.
- [2] Ullmann's Encyclopedia of Industrial Chemistry, Part A27. Triarylmethane and Diarylmethane Dyes, 6th ed., Wiley-VCH, New York, 2001.
- [3] W.W. Lee, W.H. Chung, C.S. Lu, W.Y. Lin, C.C. Chen, *Sep. Purif. Technol.* 98 (2012) 488–496.
- [4] G.L. Indig, G.S. Anderson, M.G. Nichol, J.A. Bartlett, W.S. Mellon, F. Sieber, *J. Pharm. Sci.* 89 (2000) 88–99.
- [5] B.P. Cho, T. Yang, L.R. Blankenship, J.D. Moody, M. Churchwell, F.A. Bebland, S.J. Culp, *Chem. Res. Toxicol.* 16 (2003) 285–294.
- [6] A.C. Bhasikuttan, A.V. Sapre, L.V. Shastri, *J. Photochem. Photobiol. A: Chem.* 150 (2002) 59–66.
- [7] C.Y. Chen, J.T. Kuo, H.A. Yang, Y.C. Chung, *Chemosphere* 92 (2013) 695–701.
- [8] W.H. Chung, C.S. Lu, W.Y. Lin, J.X. Wang, C.W. Wu, C.C. Chen, *Chem. Cent. J.* 6 (2012) 63.
- [9] F.D. Mai, W.L.W. Lee, J.L. Chang, S.C. Liu, C.W. Wu, C.C. Chen, *J. Hazard. Mater.* 177 (2) (2010) 864–875.
- [10] F. Chen, P. Fang, Y. Gao, Z. Liu, Y. Liu, Y. Dai, *Chem. Eng. J.* 204–206 (2012) 107–113.
- [11] K.T. Chen, C.S. Lu, T.H. Chang, Y.Y. Lai, T.H. Chang, C.W. Wu, C.C. Chen, *J. Hazard. Mater.* 174 (1–3) (2010) 598–609.
- [12] H.J. Fan, C.S. Lu, W.L.W. Lee, M.R. Chiou, C.C. Chen, *J. Hazard. Mater.* 185 (2011) 227–235.
- [13] C.C. Chen, H.J. Fan, W.H. Chung, J.L. Jan, W.Y. Lin, *J. Phys. Chem. C* 112 (31) (2008) 11962–11972.
- [14] S. Ameen, M.S. Akhtar, M. Nazim, H.S. Shin, *Mater. Lett.* 96 (2013) 228–232.
- [15] Y.H. Liao, J.X. Wang, J.S. Lin, W.H. Chung, W.Y. Lin, C.C. Chen, *Catal. Today* 174 (1) (2011) 148–159.
- [16] W.W. Lee, J. Lin, J. Chang, J. Chen, M. Cheng, C.C. Chen, *J. Mol. Catal. A: Chem.* 361–362 (2012) 80–90.
- [17] W.W. Lee, W.H. Chung, W.S. Huang, W.C. Lin, W.Y. Lin, Y.R. Jiang, C.C. Chen, *J. Taiwan Inst. Chem. Eng.* 44 (4) (2013) 660–669.
- [18] H. Xie, Y. Li, S. Jin, J. Han, X. Zhao, *J. Phys. Chem. C* 114 (2010) 9706–9712.
- [19] K. Yu, S. Yang, C. Liu, H. Chen, H. Li, C. Sun, S.A. Boyd, *Environ. Sci. Technol.* 46 (2012) 7318–7326.
- [20] C.C. Chen, W.C. Chen, M.R. Chiou, S.W. Chen, Y.Y. Chen, H.J. Fan, *J. Hazard. Mater.* 196 (2) (2011) 420–425.
- [21] H.J. Fan, S.T. Huang, W.H. Chung, J.L. Jan, W.Y. Lin, C.C. Chen, *J. Hazard. Mater.* 171 (1–3) (2009) 1032–1044.
- [22] J. Wang, Y. Yu, L. Zhang, *Appl. Catal. B: Environ.* 136–137 (2013) 112–121.
- [23] Z.T. Deng, D. Chen, B. Peng, F.Q. Tang, *Cryst. Growth Des.* 8 (2008) 2995–3003.
- [24] L. Ye, J. Chen, L. Tian, J. Liu, T. Peng, K. Deng, L. Zan, *Appl. Catal. B: Environ.* 130–131 (2013) 1–7.
- [25] K.L. Zhang, C.M. Liu, F.Q. Huang, C. Zheng, W.D. Wang, *Appl. Catal. B: Environ.* 68 (2006) 125–129.
- [26] S. Shenawi-Khalil, V. Uvarov, S. Fronton, I. Popov, Y. Sasson, *Appl. Catal. B: Environ.* 117–118 (2012) 148–155.
- [27] F. Dong, Y. Sun, M. Fu, Z. Wu, S.C. Lee, *J. Hazard. Mater.* 219–220 (2012) 26–34.
- [28] E. Keller, V. Kramer, *Z. Naturforsch.* 60b (2005) 1255–1263.
- [29] W. Wang, F. Huang, X. Lin, J. Yang, *Catal. Commun.* 9 (2008) 8–12.
- [30] S. Shenawi-Khalil, V. Uvarov, Y. Kritsmal, E. Menes, I. Popov, Y. Sasson, *Catal. Commun.* 12 (2011) 1136–1141.
- [31] J. Zhang, J. Xia, S. Yin, H. Li, H. Xu, M. He, L. Huang, Q. Zhang, *Colloids Surf. A: Physicochem. Eng. Asp.* 420 (2013) 89–95.
- [32] C. Jovalekic, M. Pavlovic, P. Osmokrovic, L. Atanasoska, *Appl. Phys. Lett.* 72 (1998) 1051–1053.
- [33] J. Wang, Y. Yu, L. Zhang, *Appl. Catal. B: Environ.* 136–137 (2013) 112–121.
- [34] J. Zhang, F. Shi, J. Lin, D. Chen, J. Gao, Z. Huang, X. Ding, C. Tang, *Chem. Mater.* 20 (2008) 2937–2941.
- [35] X. Dong, W. Ding, X. Zhang, X. Liang, *Dyes. Pigm.* 74 (2007) 470–476.
- [36] J. Cao, B. Xu, B. Luo, H. Lin, S. Chen, *Catal. Commun.* 13 (2011) 63–68.
- [37] F. Dong, W.K. Ho, S.C. Lee, Z.B. Wu, M. Fu, S.C. Zou, Y. Huang, *J. Mater. Chem.* 21 (2011) 12428–12436.
- [38] J.G. Yu, Y.R. Su, B. Cheng, *Adv. Funct. Mater.* 17 (2007) 1984–1990.
- [39] J.M. Herrmann, H. Tahiri, Y. Ait-Ichou, G. Lassaletta, A.R. Gonzalez-Elipe, A. Fernandez, *Appl. Catal. B* 13 (1997) 219–228.
- [40] C. Nasr, K. Vinodgopal, L. Fisher, S. Hotchandani, A.K. Chattopadhyay, *P.V. Kamat, J. Phys. Chem.* 100 (1996) 8436–8442.
- [41] X.P. Lin, T. Huang, F.Q. Huang, W.D. Wang, J.L. Shi, *J. Phys. Chem. B* 110 (2006) 24629–24634.
- [42] X.P. Lin, T. Huang, F.Q. Huang, W.D. Wang, J.L. Shi, *J. Mater. Chem.* 17 (2007) 2145–2150.
- [43] Q. Xiao, Z.C. Si, J. Zhang, C. Xiao, X.K. Tan, *J. Hazard. Mater.* 150 (2008) 62–67.
- [44] X. Xiao, R. Hu, C. Liu, C. Xing, X. Zuo, J. Nan, L. Wang, *Chem. Eng. J.* 225 (2013) 790–797.

- [45] S.K. Sanaa, U. Vladimir, F. Sveta, P. Inna, S. Yoel, *Appl. Catal. B: Environ.* 117–118 (2012) 148–155.
- [46] X. Xiao, R. Hao, M. Liang, X. Zuo, J. Nan, L. Li, W. Zhang, *J. Hazard. Mater.* 233–234 (2012) 122–130.
- [47] L. Chen, S.F. Yin, S.L. Luo, R. Huang, Q. Zhang, T. Hong, P.C.T. Au, *Ind. Eng. Chem. Res.* 51 (2012) 6760–6768.
- [48] S. Shenawi-Khalil, V. Uvarov, S. Fronton, I. Popov, Y. Sasson, *J. Phys. Chem. C* 116 (2012) 11004–11012.
- [49] H. Fu, C. Pan, W. Yao, Y. Zhu, *J. Phys. Chem. B* 109 (2005) 22432–22439.
- [50] S. Kim, W. Choi, *Kinetics, Environ. Sci. Technol.* 36 (2002) 2019–2025.
- [51] X. Zhu, J. Zhang, F. Chen, *Appl. Catal. B: Environ.* 102 (2011) 316–322.
- [52] F.D. Mai, C.S. Liu, J.L. Chen, C.C. Chen, *J. Chromatogr. A* 1189 (2008) 355–365.
- [53] Y. Li, H. Zhang, X. Hu, X. Zhao, M. Han, *J. Phys. Chem. C* 112 (2008) 14973–14979.